Author(s): Euclid Collaboration

Title: Euclid preparation : XV. Forecasting cosmological constraints for the Euclid and CMB joint analysis

Year: 2022

Version: Published version

Please cite the original version:

Astronomy
&
Astrophysics

Euclid preparation

XV. Forecasting cosmological constraints for the *Euclid* and CMB joint analysis

Euclid Collaboration: S. Ilić[1,2,3], N. Aghanim[4], C. Baccigalupi[5,6,7,8], J. R. Bermejo-Climent[9,10,11], G. Fabbian[12,114],
L. Legrand[4,13], D. Paoletti[10,14], M. Ballardini[10,11,15], M. Archidiacono[16,17], M. Douspis[4], F. Finelli[10,11], K. Ganga[18],
C. Hernández-Monteagudo[9,19,20], M. Lattanzi[21], D. Marinucci[22], M. Migliaccio[22,23], C. Carbone[24], S. Casas[25],
M. Martinelli[26], I. Tutusaus[3,27,28], P. Natoli[21,29], P. Ntelis[30], L. Pagano[29], L. Wenzl[31], A. Gruppuso[10,14],
T. Kitching[32], M. Langer[4], N. Mauri[14,33], L. Patrizii[14], A. Renzi[34,35], G. Sirri[14], L. Stanco[34], M. Tenti[14],
P. Vielzeuf[5,6], F. Lacasa[4], G. Polenta[36], V. Yankelevich[37], A. Blanchard[3], Z. Sakr[3,38], A. Pourtsidou[39],
S. Camera[40,41], V. F. Cardone[42,43], M. Kilbinger[25], M. Kunz[13], K. Markovic[44], V. Pettorino[25], A. G. Sánchez[45],
D. Sapone[46], A. Amara[47], N. Auricchio[10], R. Bender[45,48], C. Bodendorf[45], D. Bonino[49], E. Branchini[43,50,51],
M. Brescia[52], J. Brinchmann[53,54], V. Capobianco[49], J. Carretero[55], F. J. Castander[27,28], M. Castellano[43],
S. Cavuoti[52,56,57], A. Cimatti[58,59], R. Cledassou[60,61], G. Congedo[62], C. J. Conselice[63], L. Conversi[64,65], Y. Copin[66],
L. Corcione[49], A. Costille[67], M. Cropper[32], A. Da Silva[68,69], H. Degaudenzi[70], F. Dubath[70], C. A. J. Duncan[71],
X. Dupac[65], S. Dusini[34], A. Ealet[66], S. Farrens[25], P. Fosalba[27,28], M. Frailis[8], E. Franceschi[10], P. Franzetti[24],
M. Fumana[24], B. Garilli[24], W. Gillard[30], B. Gillis[62], C. Giocoli[72,73], A. Grazian[74], F. Grupp[45,48], L. Guzzo[16,17,75],
S. V. H. Haugan[76], H. Hoekstra[77], W. Holmes[44], F. Hormuth[78,79], P. Hudelot[80], K. Jahnke[79], S. Kermiche[30],
A. Kiessling[44], R. Kohley[65], B. Kubik[66], M. Kümmel[48], H. Kurki-Suonio[81], R. Laureijs[82], S. Ligori[49], P. B. Lilje[76],
I. Lloro[83], O. Mansutti[8], O. Marggraf[84], F. Marulli[10,14,58], R. Massey[85], S. Maurogordato[86], M. Meneghetti[10,14,87],
E. Merlin[43], G. Meylan[88], M. Moresco[10,58], B. Morin[25], L. Moscardini[10,11,58], E. Munari[8], S. M. Niemi[82],
C. Padilla[55], S. Paltani[70], F. Pasian[8], K. Pedersen[89], W. Percival[90,91,92], S. Pires[25], M. Poncet[61], L. Popa[93],
L. Pozzetti[10], F. Raison[45], R. Rebolo[9,19], J. Rhodes[44], M. Roncarelli[10,58], E. Rossetti[58], R. Saglia[45,48],
R. Scaramella[42,43], P. Schneider[84], A. Secroun[30], G. Seidel[79], S. Serrano[27,28], C. Sirignano[34,35], J. L. Starck[25],
P. Tallada-Crespí[94], A. N. Taylor[62], I. Tereno[68,95], R. Toledo-Moreo[96], F. Torradeflot[55,94], E. A. Valentijn[97],
L. Valenziano[10,14], G. A. Verdoes Kleijn[97], Y. Wang[98], N. Welikala[62], J. Weller[45,48], G. Zamorani[10], J. Zoubian[30],
E. Medinaceli[72], S. Mei[18], C. Rosset[18], F. Sureau[25], T. Vassallo[48], A. Zacchei[8], S. Andreon[75],
A. Balaguera-Antolínez[9,19], M. Baldi[10,14,15], S. Bardelli[10], A. Biviano[5,8], S. Borgani[5,7,8,99], E. Bozzo[70],
C. Burigana[11,29,100], R. Cabanac[3], A. Cappi[10,86], C. S. Carvalho[95], G. Castignani[58], C. Colodro-Conde[19],
J. Coupon[70], H. M. Courtois[101], J. Cuby[67], S. de la Torre[67], D. Di Ferdinando[14], H. Dole[4], M. Farina[102],
P. G. Ferreira[71], P. Flose-Reimberg[80], S. Galeotta[8], G. Gozaliasl[103,104], J. Graciá-Carpio[45], E. Keihanen[104],
C. C. Kirkpatrick[81], V. Lindholm[104,105], G. Mainetti[106], D. Maino[16,17,24], N. Martinet[67], M. Maturi[107,108],
R. B. Metcalf[10,15], G. Morgante[10], C. Neissner[55], J. Nightingale[85], A. A. Nucita[109,110], D. Potter[111], G. Riccio[52],
E. Romelli[8], M. Schirmer[79], M. Schultheis[86], V. Scottez[80], R. Teyssier[111], A. Tramacere[70], J. Valiviita[105,112],
M. Viel[5,6,7,8], L. Whittaker[63,113], and E. Zucca[10]

(Affiliations can be found after the references)

ABSTRACT

The combination and cross-correlation of the upcoming *Euclid* data with cosmic microwave background (CMB) measurements is a source of great expectation since it will provide the largest lever arm of epochs, ranging from recombination to structure formation across the entire past light cone. In this work, we present forecasts for the joint analysis of *Euclid* and CMB data on the cosmological parameters of the standard cosmological model and some of its extensions. This work expands and complements the recently published forecasts based on *Euclid*-specific probes, namely galaxy clustering, weak lensing, and their cross-correlation. With some assumptions on the specifications of current and future CMB experiments, the predicted constraints are obtained from both a standard Fisher formalism and a posterior-fitting approach based on actual CMB data. Compared to a *Euclid*-only analysis, the addition of CMB data leads to a substantial impact on constraints for all cosmological parameters of the standard Λ-cold-dark-matter model, with improvements reaching up to a factor of ten. For the parameters of extended models, which include a redshift-dependent dark energy equation of state, non-zero curvature, and a phenomenological modification of gravity, improvements can be of the order of two to three, reaching higher than ten in some cases. The results highlight the crucial importance for cosmological constraints of the combination and cross-correlation of *Euclid* probes with CMB data.

Key words. large-scale structure of Universe – cosmic background radiation – surveys – methods: statistical

1. Introduction

The apparent accelerated expansion of the Universe at recent cosmological epochs, revealed through the luminosity-distance relation of type Ia supernovae (SN, see Abbott et al. 2019 and references therein), and confirmed independently by the other main cosmological probes (see Planck Collaboration VI 2020; Alam et al. 2021, and references therein), is one of the greatest puzzles of modern cosmology. The ensemble of possible phenomena responsible for this acceleration constitutes the classes of dark energy (DE) and modified gravity (MG) models (see e.g. Weinberg & White in Particle Data Group 2020), often captured under the same umbrella term of 'dark energy'. Probing and unveiling the physical nature of the DE requires us to measure its effects on both the cosmological expansion and its dynamics. Both effects leave imprints at low redshift and can thus be observed through several probes, including SN, baryon acoustic oscillations (Percival 2017), the full power spectrum of galaxy clustering (GC, Wang et al. 2019) and weak lensing (WL, Munshi et al. 2020), galaxy cluster number counts (Lacasa & Rosenfeld 2016), and their cross-correlations with the cosmic microwave background (CMB, Ballardini et al. 2019a). The importance of understanding the nature of DE has triggered the development of large ground-based, photometric and/or spectroscopic galaxy surveys, such as the Kilo-Degree Survey[1] (Prole et al. 2019), the Dark Energy Survey[2] (Abbott et al. 2018a), the (extended) Baryon Oscillation Spectroscopic Survey[3] (Alam et al. 2017; Icaza-Lizaola et al. 2020), the Dark Energy Spectroscopic Instrument[4] (Dey et al. 2019), the Javalambre PAU Survey[5] (Bonoli et al. 2021), the *Vera C. Rubin* Observatory[6] (VRO, formerly the Large Synoptic Survey Telescope, Kahn 2018), and the *Roman* Space Telescope[7] (formerly the Wide Field InfraRed Survey Telescope, Akeson et al. 2019).

Joint analyses combining several or all of these low-redshift probes can lead to substantial improvement in constraining the cosmological model. Although present data are already capable of constraining the values of the parameters characterising DE to an unprecedented level (see e.g., Abbott et al. 2018b), there are still some degeneracies between these parameters and: (i) other cosmological quantities, such as the dark matter density, neutrino masses, curvature, etc.; (ii) astrophysical – or so-called nuisance – parameters involved in the models, such as (tracer) biases, mass calibration, etc.; and (iii) systematic effects, especially in extensions to the standard model. Such degeneracies can be broken by not only combining but also cross-correlating galaxy surveys with complementary cosmological probes.

Among these other data, the CMB provides us with a powerful and unique window on the early history of the Universe, as well as its geometry, dynamics, and content. The Atacama Cosmology Telescope[8] (Datta et al. 2019), the South Pole Telescope[9] (Bianchini et al. 2020), the PolarBear/Simons Array (Polarbear Collaboration 2020), and the *Planck* satellite[10] (Planck Collaboration VI 2020) already provide maps of the CMB temperature anisotropies with high signal-to-noise ratio overlapping with several ground-based galaxy surveys, thus allowing for joint analyses. Among potential studies, the cross-correlation of WL or GC with CMB lensing, which is (among other things) sensitive to the angular-diameter distance to the last-scattering surface, has been extensively explored (Holder et al. 2013; Hand et al. 2015; Kirk et al. 2016; Baxter et al. 2019). Another example can be found in cross-correlations with the thermal Sunyaev-Zeldovich (tSZ) signal, a secondary effect imprinted on top of the primordial CMB anisotropies, which has been measured with increasing precision as well (Ma et al. 2015; Hojjati et al. 2017; Osato et al. 2020; Yan et al. 2021). Additionally, several future CMB experiments, such as the Simons Observatory[11] (SO, Ade et al. 2019) and the so-called CMB-Stage 4 project[12] (CMB-S4, Abazajian et al. 2016), are planned for the next decade and will yield highly improved high-resolution measurements of the CMB intensity and polarisation. The expected improvement on the measurement of the lensing signal from the CMB photons will increase the constraining power of this probe and of its correlation with galaxy-survey-based tracers.

Within the next few years, the *Euclid* satellite[13] will be surveying the sky, mapping the large-scale structure (LSS) of the Universe with unprecedented precision, depth, and coverage. Over a volume corresponding to about $15\,000$ deg^2 on the sky and up to redshifts of $z \sim 2$, the *Euclid* Near Infrared Spectrometer and Photometer (*Euclid*-NISP) will be able to measure up to 30 million spectroscopic redshifts (Pozzetti et al. 2016), which can be used for GC measurements, while the *Euclid* Visible Instrument (*Euclid*-VIS) will measure 2 billion photometric galaxy images enabling WL observations (for more details, see Amendola et al. 2013; Laureijs et al. 2011). The unprecedented quality of the *Euclid* data will offer a new insight into the late Universe, more specifically on the growth and evolution of large-scale cosmic structures and on the expansion history of the Universe. Hence, *Euclid* data will enable us to make a leap forward in our understanding of the evolution of the late Universe and of the nature of the elusive DE.

Motivated by the need to assess the future performance of *Euclid* and its dependence on the design of the instruments, the Euclid Consortium has dedicated considerable efforts over the years towards providing reliable and realistic forecasts for the expected accuracy of cosmological measurements. First produced in the Assessment Phase Report (Refregier et al. 2010, colloquially known as the Yellow Book), and later refined in the Definition Study Report (Laureijs et al. 2011, Red Book), the *Euclid* forecasts have been recently updated by Euclid Collaboration (2020, EC20 in the following), including a comprehensive comparison of different and independent forecasting codes. EC20 updated the specifications of the satellite with a much higher degree of precision, specified in detail the assumptions used in calculations, and explored relevant cosmological models, thus providing a complete picture of the *Euclid* capabilities with respect to the late Universe observables, namely GC, WL, and their cross-correlations. Furthermore, EC20 provided a robust set of Fisher-matrix predictions, greatly improving upon previous work in terms of precision and sophistication.

In the future, not only will we jointly use WL and GC for the cosmological analysis of *Euclid* data, but we will naturally make use of the CMB information available at that time. As shown

---

[1] kids.strw.leidenuniv.nl
[2] darkenergysurvey.org
[3] sdss.org/surveys/eboss
[4] desi.lbl.gov
[5] http://www.j-pas.org/
[6] vro.org
[7] roman.gsfc.nasa.gov
[8] act.princeton.edu
[9] pole.uchicago.edu
[10] esa.int/planck

[11] simonsobservatory.org
[12] cmb-s4.org
[13] euclid-ec.org

in studies performed with CMB and ground-based survey data, the combination of the two datasets provides a great lever arm in time to constrain cosmological models. Moreover, the cross-correlations between the late-time LSS and CMB observables, arising mostly from the secondary anisotropies of CMB photons (see Aghanim et al. 2008 for a review), provide additional cosmological information at later times. Exploiting the cross-correlation between *Euclid* and the CMB data will additionally help to reduce the impact of potential systematic effects in the datasets. The exploration and preparation for this joint analysis is the raison d'être of the 'CMB cross-correlations' Science Working Group of the Euclid Consortium, responsible for the inception and the realisation of the present work.

Here, we extend the work done by EC20 and forecast the expected precision on cosmological parameters achievable from the complete combination and cross-correlation between *Euclid* and CMB data. Concerning the main *Euclid* probes, we adopt the relevant recipes and assumptions for *Euclid* GC (both spectroscopic and photometric, thereafter dubbed GCs and GCp, respectively), WL and their cross-correlations. We extend those to include CMB fields, namely total intensity, polarisation and lensing, as well as all possible *Euclid*×CMB observables, based on the same updated specifications for the *Euclid* survey.

This work is organised as follows. In Sect. 2, we describe the cosmological models considered in our forecasts and the parameters that characterise them. In Sect. 3, we introduce the Fisher matrix formalism (as well as an alternative posterior-fitting method) in order to estimate expected uncertainties on cosmological parameters, and we describe our methodology for the computation of all observables relevant to the full *Euclid*×CMB combination. In Sect. 4, we present the forecasting codes included in our analysis and describe in detail the code comparison procedure that we performed, following the same guidelines as in EC20. In Sect. 5, we present the final cosmological parameter forecasts for the *Euclid* and CMB probes, considering first the cross-correlation with the lensing signal from the CMB separately, since it is a natural counterpart to the *Euclid* probes of the LSS, and then the full joint analysis of *Euclid* and CMB probes. Finally, we present our conclusions in Sect. 6.

2. Cosmological context

This section aims to describe the different cosmological models explored in these forecasts, and their associated free parameters. The present work represents an extension and completion of the *Euclid*-only study described in EC20, hence for consistency we follow the same conventions for parameters and instrument specifications and we investigate the same cosmological models. To avoid unnecessary repetitions with EC20, we only report here some essential points for convenience, and refer the interested reader to Sect. 2 of EC20 for additional details.

The spatially flat ΛCDM model is the baseline case considered in this work; it can be described by a minimal set of six parameters. For consistency with EC20, our choice of free parameters includes: (i) the dimensionless Hubble parameter h, defined as $H_0/(100 \, \mathrm{km \, s^{1} Mpc^{1}})$ where H_0 is the Hubble rate at the present time; (ii) the total matter density parameter at present time, $\Omega_{\mathrm{m},0}$, defined as the current total matter density divided by the critical density $\rho_{\mathrm{c}} = 3H_0^2/(8\pi G)$; (iii) the same density parameter as above but for baryons, $\Omega_{\mathrm{b},0}$; (iv) the spectral index of the primordial power spectrum of scalar perturbations, denoted by n_{s}; (v) the amplitude of matter density fluctuations

at the present time through the σ_8 parameter[14]; (vi) the optical depth of reionisation τ, to which *Euclid* probes are insensitive (and thus was not considered in EC20), but which is crucial for CMB studies.

We include in this baseline model a so-called 'minimal massive neutrino' scenario (used as a baseline notably in Planck Collaboration XIII 2016), with a single massive neutrino with 0.06 eV mass and two massless neutrinos. In our analysis, this neutrino mass is never considered as a free parameter[15]. In addition to the aforementioned baseline parameters, we consider the following three extensions to the flat-ΛCDM model, each accompanied with its new parameter(s). First, we relax the assumption of spatial flatness by allowing the curvature of the Universe to be non-zero. This is equivalent to varying $\Omega_{\mathrm{DE},0}$, the DE density parameter, while both $\Omega_{\mathrm{m},0}$ and h are kept constant (see EC20 for details). Therefore, we use $\Omega_{\mathrm{DE},0}$ as a new parameter in the relevant sections of our analysis. Second, we consider the possibility of DE being dynamical in time, with a redshift-dependent equation of state $w_{\mathrm{DE}}(z)$ following the so-called CPL parametrisation (Chevallier & Polarski 2001; Linder 2003), which is $w_{\mathrm{DE}}(z) = w_0 + w_a z/(1 + z)$. Two new free parameters are thus introduced, with w_0 being the present ($z = 0$) value of the equation of state, and w_a a measure of its time variation. Finally, we allow a deviation from the standard growth of structure via a departure of the so-called growth-index parameter γ (Lahav et al. 1991; Linder 2005) from its standard value of $\gamma = 6/11$. We use this parametrisation to ease the comparison with the *Euclid* forecasts in the Red Book and for compatibility with EC20. However, although widely used, the γ parametrisation provides an incomplete and simplified description of the evolution of perturbations (which in general requires at least two degrees of freedom as a function of time and space), as also pointed out in EC20. It is valid only on sub-horizon scales and therefore not optimal for the CMB, whose observational window extends to super-horizon scales. In practice, we implemented it inside the Boltzmann codes used in our analysis, following the approach of Hojjati et al. (2011).

We summarise in Table 1 the fiducial values of all aforementioned parameters that we use throughout the present work.

3. Forecasting formalism

In this section, we give an overview of our forecasting formalism and define specific quantities that are used throughout this work. We also present the detailed recipes we adopted during our implementation of the Fisher matrix formalism, and for the computation of forecasts of the different cosmological probes considered in the joint *Euclid*×CMB analysis.

3.1. General Fisher formalism

We are interested in quantifying the ability of *Euclid* and CMB data to constrain the parameters of our minimal ΛCDM cosmological model and several of its extensions (see Sect. 2). In order to do so, we use a standard Fisher matrix approach (Bunn 1995; Vogeley & Szalay 1996; Tegmark et al. 1997) where the elements of the Fisher matrix F are defined as (minus) the expectation value of the second derivative of the natural logarithm of

---

[14] We note that this parameter is often dropped in favour of A_{s} when considering CMB observables.

[15] EC20 verified that another choice for the neutrino mass (within a reasonable range permitted by current data) leads to nearly no change in cosmological forecasts.

Table 1. Fiducial values of the cosmological parameters considered.

	Baseline						Extensions			
$\Omega_{\rm b,0}$ $(\omega_{\rm b,0})$	$\Omega_{\rm m,0}$ $(\omega_{\rm m,0})$	h	$n_{\rm s}$	σ_8	τ	$\sum m_\nu$ [eV] (fixed)	$\Omega_{\rm DE,0}$	w_0	w_a	γ
0.05 (0.022445)	0.32 (0.143648)	0.67	0.96	0.816	0.058	0.06	0.68	-1	0	6/11

Notes. We show here the parameter values of our fiducial cosmological model, both in the baseline-ΛCDM case and in the extensions that we consider. Values are chosen to be identical to the ones in EC20. As mentioned in the text, it should be noted that for non-flat cosmological models, $\Omega_{\rm DE,0}$ is also varied in conjunction with $\Omega_{\rm K,0}$ (so as to keep all other parameters constant).

the likelihood $\mathcal{L}$ with respect to the model parameters of interest (denoted θ_i here), evaluated at their fiducial values $\theta_{i,\rm fid}$:

$$F_{\alpha\beta} = -\left\langle \frac{\partial^2 \ln \mathcal{L}}{\partial \theta_\alpha \partial \theta_\beta} \right\rangle \Bigg|_{\theta_i = \theta_{i,\rm fid}}. \tag{1}$$

The inverse of the resulting Fisher matrix is then a good approximation of the covariance of the posterior distribution of model parameters (that one would have obtained via for example standard Markov chain Monte Carlo techniques, hereafter MCMC), ensemble-averaged over many realisations of the data. If the probability distribution of the observables used to build the likelihood is Gaussian, then the Fisher matrix can be computed analytically:

$$F_{\alpha\beta} = \frac{1}{2} {\rm Tr}\left[\mathsf{C}^{-1} \frac{\partial \mathsf{C}}{\partial \theta_\alpha} \mathsf{C}^{-1} \frac{\partial \mathsf{C}}{\partial \theta_\beta} \right] + \frac{\partial \boldsymbol{\mu}^{\mathsf{T}}}{\partial \theta_\alpha} \mathsf{C}^{-1} \frac{\partial \boldsymbol{\mu}}{\partial \theta_\beta}, \tag{2}$$

where Tr stands for the trace operator for a (square) matrix, $\boldsymbol{\mu}$ is the vector of expectation values for the observables considered, C is their theoretical covariance, and all derivatives are evaluated at the fiducial point $\theta_{i,\rm fid}$. In the present study, our observables are the estimates – denoted by $\hat{C}_\ell^{\mathcal{X}\mathcal{Y}}$ – of all possible angular auto- and cross-power spectra with observables $\mathcal{X}$ and $\mathcal{Y}$ drawn from the following list: CMB temperature; CMB polarisation (E modes only); CMB lensing; GCp[16]; and WL. Consequently, the $\boldsymbol{\mu}$ vector is a concatenation of the theoretical expectations $C_\ell^{\mathcal{X}\mathcal{Y}} \equiv \langle \hat{C}_\ell^{\mathcal{X}\mathcal{Y}} \rangle$ of these estimated angular spectra, and the C matrix corresponds to their covariance (cf. Eq. (16)), which includes the expected sources of error in the context of the various experiments we considered (see the next section for more details about the computation of those quantities). We note that, in practice, we keep only the second term of Eq. (2) when computing our Fisher matrices. This is due to the fact that our observables, $\hat{C}_\ell^{\mathcal{X}\mathcal{Y}}$, do not follow a Gaussian distribution but a Wishart one; properly deriving the Fisher formula for such a distribution (starting from Eq. (1)) leads to a formula identical to Eq. (2) but without the leftmost term (see e.g. Carron 2013; Bellomo et al. 2020).

Once the Fisher matrix is computed, an estimate of the covariance matrix M of our model parameters[17] is given by

$$\mathsf{M}_{\alpha\beta} = (\mathsf{F}^{-1})_{\alpha\beta}, \tag{3}$$

and the square root of its diagonal elements yields the 1σ marginalised uncertainties on each parameter:

$$\sigma_\alpha = \sqrt{\mathsf{M}_{\alpha\alpha}}. \tag{4}$$

---

[16] GCs is considered as an independent probe, and its Fisher matrix is directly added to our final computation using the publicly available results of EC20. See also the last paragraph of Sect. 3.2.

[17] More specifically, by virtue of the Cramér-Rao inequality, we obtain a lower bound on the covariance of our parameters.

We note that in order to combine the *Euclid* Fisher matrices with current CMB constraints (mainly *Planck* in our case), the computation of theoretical CMB power spectra is required. These spectra can be made to reproduce as much as possible the characteristics (noise level, beams, etc.) of the actual existing CMB data, and should be computed using the same fiducial model as the one used for the *Euclid* Fisher matrices. However, one may argue that this method may not accurately reproduce all the nuances of the actual CMB data. As a matter of fact, best-fit values of cosmological parameters for the *Planck* data have already been determined, and slightly differ (depending on the exact dataset used) from the ones chosen by EC20 to build the *Euclid* Fisher matrices. Moreover, the actual full *Planck* likelihood is available and has been thoroughly sampled via MCMC methods. We discuss in Sect. 3.6 an alternative to traditional Fisher forecasting, making use of real CMB data. We stress, however, that this method is not be applicable when considering forecasts involving future CMB surveys.

3.2. Recipe for the Euclid observables

As mentioned in Sect. 3.1, building our Fisher matrix implies the computation of the theoretical expectation values of the set of observables (for our fiducial models) as well as their expected covariances and derivatives with respect to the considered model parameters. Regarding the main *Euclid* cosmological probes – namely photometric and spectroscopic galaxy clustering (GCp and GCs), WL, and the cross-correlation between GCp and WL – recipes for their computation are explained in great detail in Sect. 3 of EC20. We summarise here the main points, and focus on the specific aspects relevant to our endeavour.

Thanks to the unprecedented precision and depth of the future *Euclid* survey, the WL and GC signals are expected to be measured well over a series of redshift bins; in our analysis, we consider five and ten photometric bins, respectively, for the pessimistic and optimistic Euclid scenarios. The theoretical modelling of the WL, GCp and cross-correlation power spectra in each of those redshift bins consists of computing integrals of the following form, assuming the flat-sky and Limber approximations:

$$C_\ell^{\mathcal{X}\mathcal{Y}} = c \int \frac{{\rm d}z}{H(z)r^2(z)} \mathcal{W}^{\mathcal{X}}(z)\, \mathcal{W}^{\mathcal{Y}}(z)\, P_{\delta\delta}\left(\frac{\ell+1/2}{r(z)}, z \right) + \mathcal{N}_\ell^{\mathcal{X}\mathcal{Y}}. \tag{5}$$

In the above expression, the letters $\mathcal{X}$ and $\mathcal{Y}$ can stand either for WL$_i$ or GCp$_i$ (the subscript i referring to the ith redshift bin considered) and $\mathcal{W}^{\mathcal{X}}$ represents the so-called 'kernel' associated with observable $\mathcal{X}$. For WL, this kernel includes contributions from both the cosmic shear signal (γ) and the intrinsic alignment

Table 2. Specifications for the *Euclid* photometric survey.

	Parameter	*Euclid*
Survey area in the sky	A_{survey}	$15\,000 \text{ deg}^2$
Sky fraction	f_{sky}	0.36
Galaxy number density	n_g	30 arcmin^{-2}
Total intrinsic ellipticity dispersion	σ_ϵ	0.30
Minimum (measured) redshift	z_{min}	0.001
Maximum (measured) redshift	z_{max}	0.9 (pessimistic), 2.5 (optimistic)
Number of redshift bins	N_z	5 (pessimistic), 10 (optimistic)
Minimum multipole (WL and GC)	ℓ_{min}	10
Maximum multipole for WL	ℓ_{max}	1500 (pessimistic), 5000 (optimistic)
Maximum multipole for GC	ℓ_{max}	750 (pessimistic), 3000 (optimistic)

(IA) systematic effect, and can be written as

$$\mathcal{W}^{\text{WL}_i}(z) = \mathcal{W}^{\gamma_i}(z) - \frac{\mathcal{P}_{\text{IA}}\Omega_{\text{m},0}}{D(z)}\mathcal{W}^{\text{IA}_i}(z)\,, \quad (6)$$

with

$$\mathcal{W}^{\gamma_i}(z) = \frac{3}{2}\frac{H_0^2}{c^2}\Omega_{\text{m},0}\,(1+z)\,r(z)\int_z^\infty \text{d}z'\,\frac{n_i(z')}{\bar{n}_i}\left[1 - \frac{r(z)}{r(z')}\right]\,, \quad (7)$$

$$\mathcal{W}^{\text{IA}_i}(z) = \frac{n_i(z)}{\bar{n}_i}\frac{H(z)}{c}\,. \quad (8)$$

The kernel corresponding to the GCp is

$$\mathcal{W}^{\text{GCp}_i}(z) = b_i(z)\frac{n_i(z)}{\bar{n}_i}\frac{H(z)}{c}\,. \quad (9)$$

In these expressions, $n_i(z)$ stands for the observed number density of galaxies in the ith redshift bin. It is given by the convolution of the true galaxy distribution $n(z)$ with the photometric redshift error, the latter being characterised by the probability $p_{\text{ph}}(z_\text{p}|z)$ of a galaxy at a (true) redshift z to be measured via photometry at a redshift z_p. Furthermore, $\bar{n}_i$ is the galaxy surface density normalising $n_i(z)$ and $D(z)$ is the linear growth factor. $\mathcal{P}_{\text{IA}}$ encapsulates a specific intrinsic alignment model described in EC20, and introduces three nuisance parameters named $\mathcal{A}_{\text{IA}}$, η_{IA} and β_{IA} in the Fisher analyses. The specific forms of all the aforementioned functions are given in EC20, and we note that all parameters of the redshift distribution and photometric error models are fixed to their fiducial value in our analysis. The galaxy bias $b_i(z)$ is assumed to be scale-independent and constant in any given redshift bin, with fiducial values $b_i = \sqrt{1 + z_{\text{c},i}}$, where $z_{\text{c},i}$ is the central redshift of the ith bin. The resulting 10 bias parameters b_i are part of the present Fisher analysis, where they are considered as nuisance parameters. The function $H(z)$ is the usual Hubble rate as a function of redshift z. The total matter power spectrum $P_{\delta\delta}$ is evaluated at $k = (\ell + 1/2)/r(z)$ in accordance with the Limber approximation, where $r(z)$ is the comoving distance as a function of redshift:

$$r(z) = c\int_0^z \frac{\text{d}z'}{H(z)}\,. \quad (10)$$

Measurements by *Euclid* will extend down to small scales where clustering enters the non-linear regime. As a consequence, the non-linear corrections of `Halofit` (Takahashi et al. 2012), as well as the neutrino corrections of Bird et al. (2012), are included in $P_{\delta\delta}$. Finally, $\mathcal{N}_\ell^{\mathcal{X}\mathcal{Y}}$ contains the shot-noise term:

$$\mathcal{N}_\ell^{\mathcal{X}\mathcal{Y}} = \frac{\sigma^2}{\bar{n}_i}\,, \quad (11)$$

where $\sigma = \sigma_\epsilon$ (the total intrinsic ellipticity dispersion) when $\mathcal{X} = \mathcal{Y} = \text{WL}_i$, $\sigma = 1$ when $\mathcal{X} = \mathcal{Y} = \text{GCp}_i$, and 0 otherwise. The shot-noise amplitude is fixed throughout the analysis (and thus is not part of the nuisance parameters).

We should note that, in practice, some of the numerical codes used in the present analysis do not directly use the expression shown in Eq. (5) – as detailed in Sect. 4. Indeed, since CMB observables are also required in our analysis, and provided that the Limber approximation cannot be applied to the computation of such observables, the following expression was used instead:

$$C_\ell^{\mathcal{X}\mathcal{Y}} = 4\pi\int_0^\infty \text{d}r_1\,\mathcal{W}^{\mathcal{X}}(r_1)\int_0^\infty \text{d}r_2\,\mathcal{W}^{\mathcal{Y}}(r_2)$$
$$\times \int_0^\infty \frac{\text{d}k}{k}\,\mathcal{P}_{\mathcal{R}}(k)\,T_{\mathcal{X}}(k,r_1)\,j_\ell(kr_1)\,T_{\mathcal{Y}}(k,r_2)\,j_\ell(kr_2)\,. \quad (12)$$

This formula involves the use of more general scale- and time-dependent 'transfer functions' $T(k,r)$: they characterise the time evolution (at any given scale k) of a perturbation of the cosmological quantity sourcing the considered observable, for example in the case of GCp the perturbation of the matter density field. Those functions are then multiplied by the primordial curvature power spectrum ($\mathcal{P}_{\mathcal{R}}$) instead of the total matter power spectrum $P_{\delta\delta}$. These transfer functions usually do not have a closed-form expression and require the use of Boltzmann codes to be computed. The presence of additional integrals involving spherical Bessel functions (j_ℓ) renders this expression much more computationally expensive. However, it holds for both *Euclid* and CMB observables, as well as their inter- and intra-cross-correlations.

We report in Table 2 the specifications used to construct the aforementioned WL and GCp angular power spectra. In the present analysis, we consider two scenarios for the *Euclid* probes: an optimistic case, where ten equally populated redshift bins (ranging from $z = 0$ to 2.5) are exploited and the multipole range extends from $\ell_{\min} = 10$ to 3000 and 5000 (for GCp and WL, respectively); a more pessimistic case, where only five redshift bins (up to $z = 0.9$) are considered and the highest multipole is reduced to $\ell = 750$ and 1500 respectively. A visual representation of the aforementioned redshift bins is shown in Fig. 1, while the exact binning scheme can be found in EC20.

As a final note, in accordance with the approach of EC20, we consider GCs as an independent probe (thus uncorrelated to all other probes considered) throughout our whole analysis. The contribution of GCs to our final Fisher matrices is therefore accounted for via the simple addition of the corresponding Fisher matrix published by the Euclid Collaboration. The full recipe for the GCs observables is detailed in EC20 and consists of the full, anisotropic, and redshift-dependent galaxy power spectrum to
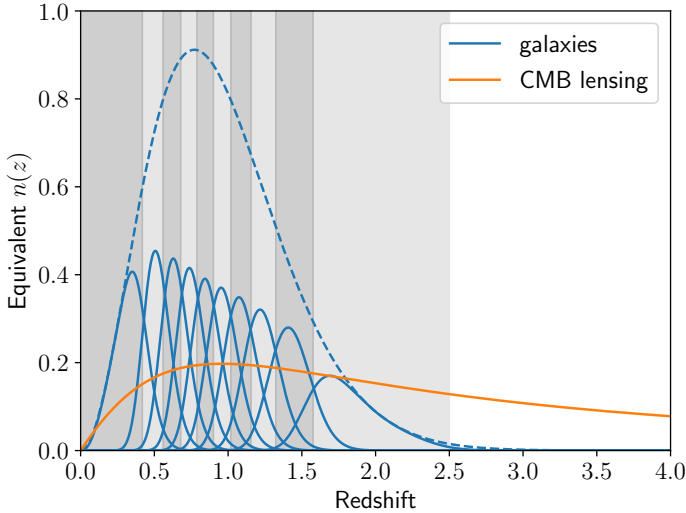
Fig. 1. Redshift distribution (normalised to unit area) assumed for the galaxies of the *Euclid* photometric sample in dashed blue; the grey bands indicate the ten (observed) redshift bins used in the analysis, and the solid blue curves show the ten corresponding true underlying redshift distributions. The solid orange curve shows the equivalent redshift distribution (also normalised to unit area) derived from the CMB lensing kernel of Eq. (15) for our fiducial cosmological model.

be derived from the *Euclid* spectroscopic galaxy sample. A pessimistic and optimistic version of GCs is also considered.

3.3. Recipe for CMB observables

We consider the information available in CMB data by using power spectra from temperature and *E* mode polarisation anisotropies and CMB lensing. We do not include the *B* mode polarisation since it does not add information for scalar perturbations. Our choice of observables are the various angular auto- and cross-spectra computed from those signals: C_ℓ^{TT}, C_ℓ^{TE}, C_ℓ^{EE}, $C_\ell^{\phi\phi}$, $C_\ell^{T\phi}$, $C_\ell^{E\phi}$ (where T, E and ϕ respectively stand for the CMB temperature, *E* mode polarisation and lensing signals). The computation of those power spectra is taken care of by dedicated Boltzmann codes in our analysis, namely the popular and well-tested CLASS and CAMB public codes (see Sect. 4 for more details).

Similarly to *Euclid* observables, we contemplated a variety of scenarios for the characteristics of the CMB observables considered: a *Planck*-like (nearly) full-sky survey and two types of ground-based observatories based on actual future experiments, namely the SO and CMB-S4. In the latter two cases, the fraction of the sky expected to be covered will be of order 40%, translating into a lower bound of $\ell \simeq 40$ for the available range of multipoles for temperature and polarisation. In order to avoid neglecting the precious amount of information contained in the CMB at large scales (and their exquisite measurement by *Planck*), our hypothetical two ground-based scenarios also assume that constraints from the *Planck* large-scale temperature and polarisation signals are included, via the addition of the corresponding C_ℓs from *Planck* in the Fisher analysis for multipoles $\ell < 40$. We stress, however, that measurement of the CMB lensing on such large scales is not prevented (though it is noisier) by the restricted sky fraction, thanks to the process through which the signal is recovered – namely via high-order T and E correlations on small angles, to which all scales of the lensing signal contribute and can thus be inferred. As a consequence, for

ground-based experiments we consider the full range of multipoles (starting from $\ell = 2$) coming solely from the chosen experiments for CMB lensing.

Regarding the specifications of CMB measurements in all three scenarios, we adopt for the C_ℓ^{TT} and C_ℓ^{EE} spectra an isotropic noise deconvolved with the instrument beam (Knox 1995):

$$\mathcal{N}_\ell^{XX} = w_{XX}^{-1}\, b_\ell^{-2}, \qquad b_\ell = \exp\left(-\frac{1}{2}\,\ell\,(\ell+1)\,\frac{\theta_{\mathrm{FWHM}}^2}{8\ln 2}\right), \qquad (13)$$

where θ_{FWHM} is the full-width-at-half-maximum (FWHM) of the beam given in radians and w_{TT}, w_{EE} are the inverse square of the detector noise levels (ΔT and ΔE) in µK arcmin, for temperature and polarisation, respectively. The total noise for multiple frequency channels is given by their inverse noise-weighted sum. To estimate the CMB lensing noise, we reconstruct the minimum-variance estimator for $\mathcal{N}_\ell^{\phi\phi}$ (Okamoto & Hu 2003) by using the publicly available code quicklens[18] and the noise estimates $\mathcal{N}_\ell^{\mathrm{TT}}$ and $\mathcal{N}_\ell^{\mathrm{EE}}$.

3.3.1. *Planck*

For simulating our *Planck*-like experiment, we aim to reproduce the *Planck* 2018 results for the ΛCDM model. Our target is the corresponding baseline data combination consisting of temperature, polarisation (Planck Collaboration V 2020), and lensing likelihoods (Planck Collaboration VIII 2020) released by the Planck Collaboration. Due to the complexity of the actual *Planck* data and likelihood, we have tailored the noise model and parameters in order to reproduce the real data likelihood-based uncertainties (Planck Collaboration V 2020) with the Fisher formalism. In summary, we use the sensitivity specifications of the 143-GHz channel of the HFI instrument (Planck Collaboration I 2016) with a sky fraction $f_{\mathrm{sky}} = 0.7$ and a maximum multipole $\ell_{\max} = 1500$ for TT, TE, EE. In order to reproduce the (systematic-dominated) optical depth uncertainty, we inflate $\mathcal{N}_\ell^{\mathrm{EE}}$ by a factor of eight for $\ell < 30$ (Bermejo-Climent et al. 2020). The *Planck*-like effective noise for the CMB lensing power spectrum is obtained through the specifications of the 143 GHz and 217 GHz channels in Planck Collaboration I (2016). The CMB lensing power spectrum $C_\ell^{\phi\phi}$ uses a conservative range, namely $8 \le \ell \le 400$ (Planck Collaboration VIII 2020).

3.3.2. Simons Observatory

The SO was initiated in 2016 with the goal of mapping the CMB with three 50-cm-class refracting imagers and one 6-m telescope at an altitude of 5200 m in the Chilean Andes. This 6-m telescope will produce data appropriate for combination and cross-correlation with *Euclid*. First-light is expected in 2022, with science operations beginning in 2023. It will ultimately cover a usable fraction of the sky of 40% (cf. Fig. 2) with beam FWHM between 0.9 and 7.4 arcmin over the frequency range from 27 through 280 GHz. Over the six bands spanning this frequency range, the temperature noise expectations are 71 to 54 µK arcmin, while the goals are a factor of $\sqrt{2}$ better (Ade et al. 2019). Figure 2 compares the sky coverage of *Euclid* and SO. We use in our Fisher analysis the noise curves provided by the SO Collaboration in Ade et al. (2019)[19]. In practice,

---

[18] github.com/dhanson/quicklens

[19] We use the version 3.1.0 available at github.com/simonsobs/so_noise_models.
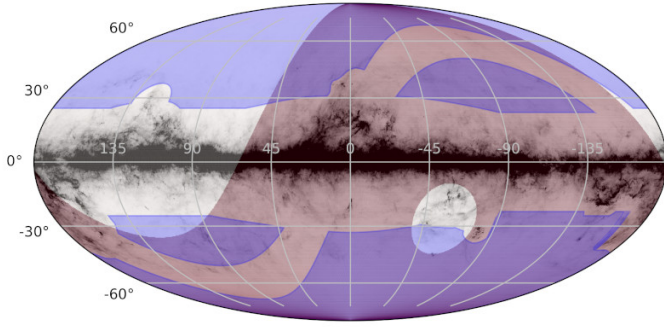
Fig. 2. Comparison of *Euclid* and SO sky coverage in Galactic coordinates. The blue, semi-transparent regions covering most of the northern and southern Galactic hemispheres away from the Galactic plane is the currently planned *Euclid* sky coverage (Scaramella et al., in prep.). In addition to a Galactic cut, *Euclid* also avoids regions within about 15° of the ecliptic plane, seen here as the band running from the lower, left-hand part of the graphic to the upper, right-hand part. The region covering most of the right of the plot (with a light red hue) indicates the sky available to SO, assuming a minimum observation elevation of 40°. Roughly 70% of the celestial sphere is accessible to SO, though this is reduced to around 40% when one makes reasonable Galactic cuts. The underlying, grey-scale map shows the Planck 545-GHz map, which gives one an indication of what regions are most contaminated by thermal emission from Galactic dust.

we take the noise curves obtained with the ILC component-separation method, assuming the baseline analysis for a sky fraction of 0.4 (see Fig. 2). We differ here from the formula used for *Planck*, since the SO noise is modelled using the component-separation method for all channels. For our forecasts with SO, we use data over $40 \leq \ell \leq 3000$ for TT and TE, $40 \leq \ell \leq 5000$ for EE, and $2 \leq \ell \leq 3000$ for $\phi\phi$ and Tϕ. As mentioned at the beginning of Sect. 3.3, this scenario also considers the addition of large-scale data from the *Planck* survey; in practice, we add this information via the first multipoles of all T- and E-related spectra considered, up to $\ell = 40$, with the same specifications as described earlier for the *Planck*-like survey.

3.3.3. CMB-Stage 4

The CMB-S4 experiment, which will follow the SO (in combination with the successors to the South Pole Telescope and the current BICEP/Keck collaboration in Antarctica) is scheduled to begin taking data in 2027. We assume that it will have an additional dedicated large-aperture telescope similar to that of SO described above (Abazajian et al. 2016) and, given more stringent foreground requirements, will also cover 40% of the sky, although with improved depth. We use $\Delta T = 1\,\mu\mathrm{K}$ arcmin, $\Delta E = \sqrt{2}\,\mu\mathrm{K}$ arcmin and $\theta_{\mathrm{FWHM}} = 1\,\mu\mathrm{K}$ arcmin. CMB-S4 is expected to use data over $40 \leq \ell \leq 3000$ in temperature and $40 \leq \ell \leq 5000$ in polarisation. The lensing power spectrum will use data from $2 \leq \ell \leq 3000$, and its noise curve is taken as the so-called N0 bias (see e.g., Carron & Lewis 2017), which is computed using the `quicklens` code. Similarly to the SO case, *Planck*-like large-scale information is also added in this scenario. We note that one can expect to improve upon the noise level since it is estimated by the Okamoto & Hu (2003) method, notably by using iterative delensing (see e.g., Schmittfull & Seljak 2018). Therefore, the results shown in the present work should be thought as being conservative and a lower bound on the constraints obtainable from CMB lensing.

All specifications for our three considered CMB experiments are summarised in Table 3, and the noise curves for all CMB auto-spectra are shown in Fig. 3.

3.4. Recipe for Euclid×CMB observables

The computation of the *Euclid*×CMB observables (namely, all possible combinations of the GCp or WL measurements with the T, E, or ϕ signals) can be performed in principle by using either of the two angular spectra equations described in Sect. 3.2, namely Eq. (5) and Eq. (12). In practice, due to the non-trivial nature of their transfer functions, any combination involving T or E cannot be performed via the simplified, Limber-approximated Eq. (5) and thus requires the use of Eq. (12) – together with a Boltzmann code. We note, however, that due to the mostly late-time nature of the CMB lensing signal, combinations involving ϕ can use the simplified formula for cross-spectra, using the following scale-independent CMB lensing kernel:

$$\mathcal{W}^{\phi}(z) = \frac{3}{2}\frac{H_0^2}{c^2}\,\Omega_{\mathrm{m},0}\,(1+z)\,r(z)\left[1 - \frac{r(z)}{r(z^*)}\right], \tag{14}$$

where $r(z^*)$ is the comoving distance to the surface of last scattering at redshift z^* (see e.g., Lewis & Challinor 2006). For comparison purposes, one can derive from the CMB lensing kernel an equivalent of the redshift distribution present in the GC kernel in Eq. (10):

$$\mathcal{W}^{\phi}(z) \equiv \frac{n_\phi(z)}{\bar{n}_\phi}\frac{H(z)}{c} \;\Rightarrow\; \frac{n_\phi(z)}{\bar{n}_\phi} \equiv \mathcal{W}^{\phi}(z)\frac{c}{H(z)}. \tag{15}$$

We show the resulting n_ϕ in Fig. 1 for comparison with the GC redshift distributions used in our analysis.

In total, we thus consider six cross-correlation signals between *Euclid* and CMB probes, namely GCp×T, GCp×E, GCp×ϕ, WL×T, WL×E, and WL×ϕ. We stress that for all cross-signals involving WL, we properly account for the fact that the WL kernel is composed of a shear (γ) part and an IA part (cf. Sect. 3.2) and that each correlates differently to CMB observables.

3.5. Fisher-matrix implementation

A key component required for the computation of Fisher matrices is the covariance matrix of the considered observables. We restrict ourselves to a Gaussian formulation of the covariance between estimated angular power spectra, which is given by

$$\mathrm{Cov}\left[\hat{C}_\ell^{\mathcal{XY}},\hat{C}_{\ell'}^{\mathcal{X'Y'}}\right] = \frac{\delta_{\ell\ell'}^{\mathrm{K}}}{(2\ell+1)f_{\mathrm{sky}}}$$
$$\times\left\{\left[C_\ell^{\mathcal{XX'}} + \mathcal{N}_\ell^{\mathcal{XX'}}\right]\left[C_{\ell'}^{\mathcal{YY'}} + \mathcal{N}_{\ell'}^{\mathcal{YY'}}\right]\right.$$
$$\left. + \left[C_\ell^{\mathcal{XY'}} + \mathcal{N}_\ell^{\mathcal{XY'}}\right]\left[C_{\ell'}^{\mathcal{YX'}} + \mathcal{N}_{\ell'}^{\mathcal{YX'}}\right]\right\}, \tag{16}$$

where δ^{K} is the Kronecker delta, meaning that we assume no correlations between different multipoles. The indices $\mathcal{X}$, $\mathcal{Y}$, $\mathcal{X'}$ and $\mathcal{Y'}$ can be any of the observables considered, namely T, E, ϕ, WL_i or GCp_i. The noise terms for auto-spectra are described in Sects. 3.2 and 3.3, while all cross-spectra are assumed to have zero noise; this assumption holds as long as no given systematic effect contributes to the corresponding combination of observables. We make a conservative choice for the value of the sky fraction f_{sky} in Eq. (16) by setting it each time to the smallest fraction among the four $\mathcal{X}$, $\mathcal{Y}$, $\mathcal{X'}$ and $\mathcal{Y'}$ observables.

Table 3. Specifications for CMB experiments.

	Parameter	*Planck*	Simons observatory + *Planck* low-ℓ	CMB+Stage 4 + *Planck* low-ℓ
Sky fraction	$f_{\rm sky}$	0.7	0.4	0.4
Beam FWHM	$\theta_{\rm FWHM}$	7 arcmin	2 arcmin	1 arcmin
Temperature noise	$\Delta {\rm T} \equiv (w_{\rm TT})^{-1/2}$	23 µK arcmin	3 µK arcmin	1 µK arcmin
Polarisation noise	$\Delta {\rm E} \equiv (w_{\rm EE})^{-1/2}$	42 µK arcmin	$3\sqrt{2}$ µK arcmin	$\sqrt{2}$ µK arcmin
TT multipole range	$[\ell_{\rm TT,min}, \ell_{\rm TT,max}]$	[2, 1500]	[2, 3000]	[2, 3000]
TE multipole range	$[\ell_{\rm TE,min}, \ell_{\rm TE,max}]$	[2, 1500]	[2, 3000]	[2, 3000]
EE multipole range	$[\ell_{\rm EE,min}, \ell_{\rm EE,max}]$	[2, 1500]	[2, 5000]	[2, 5000]
$\phi\phi$ multipole range	$[\ell_{\phi\phi,min}, \ell_{\phi\phi,max}]$	[8, 400]	[2, 3000]	[2, 3000]
$T\phi$ multipole range	$[\ell_{{\rm T}\phi,min}, \ell_{{\rm T}\phi,max}]$	[8, 400]	[2, 3000]	[2, 3000]

Given those assumptions, we can rewrite the Fisher matrix expression in Eq. (2) as a sum of independent Fisher matrices, one per multipole:

$$\mathsf{F}_{\alpha\beta} = \sum_\ell \mathsf{F}_{\alpha\beta,\ell}\,, \qquad (17)$$

where for a given multipole ℓ, the 'partial' Fisher matrix $\mathsf{F}_{\alpha\beta,\ell}$ is given by (see details in Sect. 3.1)

$$\mathsf{F}_{\alpha\beta,\ell} = \frac{\partial \boldsymbol{\mu}^{\mathsf{T}}}{\partial \theta_\alpha} \mathsf{C}^{-1} \frac{\partial \boldsymbol{\mu}}{\partial \theta_\beta}\,. \qquad (18)$$

In this expression, the vector $\boldsymbol{\mu}$ contains all possible auto- and cross-power spectra $C_\ell^{\mathcal{X},\mathcal{Y}}$ derivable from the considered probes for that particular multipole ℓ, while C is the covariance matrix of the estimated $\hat{C}_\ell^{\mathcal{X},\mathcal{Y}}$ computed via Eq. (16).

3.6. Fitted-Fisher approach

As a complement to (and a form of validation of) the traditional Fisher-matrix methodology, we also adopted an alternative technique, referred to as the 'fitted-Fisher approach'. It is designed to combine a theoretical Fisher matrix, such as the one computed for *Euclid*, with likelihood constraints from actual data – in our case, CMB data from the *Planck* satellite. A detailed description of the method, as well as the associated results and discussion, can be found in Appendix A. Overall we find a good agreement between the use of the actual Planck data and the standard Fisher forecast described in Sects. 3.1–3.5.

4. Numerical tools

This section presents the description and validation of the Fisher matrix codes used in this work, each of which provides an implementation of the formalism described in Sect. 3, assuming the various cosmological models given in Sect. 2. The codes are capable of computing two of the *Euclid* main probes (GCp and WL) as well as CMB observables (temperature, polarisation, and lensing), and have been specifically optimised for computing the cross-correlations between the two. They follow the *Euclid* and CMB survey specifications outlined earlier.

4.1. Code descriptions

As a starting point, we provide in the following a brief description of each code, highlighting their main features.

Several programming languages and approaches have been adopted, thus providing a way to test the robustness of results against implementation choices. The codes are interfaced with different Boltzmann solvers widely used by the cosmological community, namely either `CAMB sources`[20] or `CLASS`[21] (Blas et al. 2011), which adds another layer of validation to our results. `CosmicFish`[22] (Raveri et al. 2016a,b) and `CosmoSIS`[23] (Zuntz et al. 2015) are two of the codes that were employed in EC20, validated against a number of additional codes in the context of computing forecasts for the main *Euclid* probes. As a consequence, those codes have not been designed to compute CMB and *Euclid*×CMB observables. Nonetheless, they were used in the present work as references for the computation of *Euclid* observables. Full details of the two codes can be found in EC20.

`BolFish`[24] is a Fisher matrix code for CMB and LSS now written in Python 3 (Bermejo-Climent et al. 2021) and used in its previous implementations in Ballardini et al. (2016, 2019b). In its basic settings, it interfaces with a modified version of `CAMB sources`, which allows for the introduction of survey specifications (such as the number density of galaxies or the galaxy bias function), nuisance parameters and tomography. The `BolFish` code is also able to work with angular power spectra for CMB anisotropy fields, galaxy counts and their cross-correlation, or with the matter power spectrum $P(k)$ provided as external inputs. `BolFish` allows the exploration of several extensions to the standard ΛCDM model, such as the CPL DE parametrisation or massive neutrinos. By default, numerical derivatives are computed with a three-point stencil method, where the step size for each parameter is user-defined. This Fisher code allows the use of different settings (e.g. ℓ range) for the different angular power spectra considered, which is useful when performing a joint 2D analysis of CMB and LSS probes.

`SFX-CLASS`[25] comprises a customised version of the `CLASS` Boltzmann code, optimised for the purpose of computing LSS and LSS×CMB observables. It is broadly compatible with any LSS survey specifications and adds the computation of systematic effects such as intrinsic alignments for WL calculations. It supports all cosmological models implemented in the standard version of `CLASS`, and is theoretically expandable to all extensions of `CLASS` that have been developed in the literature. It is also interfaced with a user-friendly Fisher-matrix code

---

[20] `camb.info/sources`
[21] `class-code.net`
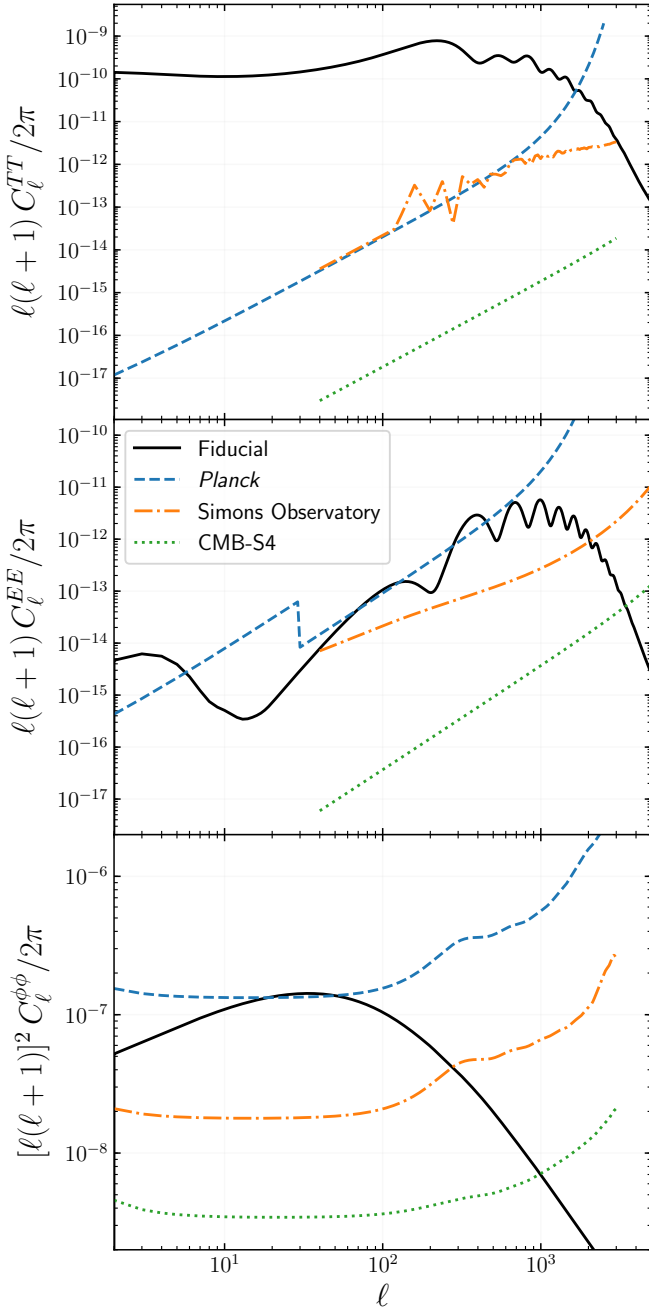[22] `cosmicfish.github.io`
[23] `bitbucket.org/joezuntz/cosmosis`
[24] Contact: J. R. Bermejo-Climent.
[25] Contact: S. Ilić.

Fig. 3. Noise power spectra used to reproduce the CMB experiments considered. We show the noise curves for *Planck* (dashed blue lines), SO (dash-dotted orange lines), and CMB-S4 (dotted green lines), as well as our fiducial C_ℓ for reference in black. *Top, middle, and bottom panels*: correspond, respectively, to the temperature, polarisation (we note the inflated noise at $\ell < 30$ for the *Planck*-like case, cf. Sect. 3.3.1) and CMB lensing signals. Only auto-power spectra are shown, since we neglect the noise for the cross-correlation between CMB signals.

(written in Python), dedicated to performing the repeated calls to the aforementioned modified CLASS code, which are required to obtain the derivatives of the observables under consideration. It computes these derivatives via either a standard three-point stencil method or a polynomial fit of arbitrary order over an arbitrary number of points (respectively fixed to 2 and 21 in the present work) around the chosen fiducial point.

PyCross[25] is a standalone Python code, interfaced with a standard version of the CLASS code. It takes care of the com-

putation of the angular power spectra for LSS and LSS×CMB observables itself, combining intermediate outputs from CLASS (such as the matter power spectrum) and LSS survey specifications, without using the Limber approximation. Its main feature is the use of the so-called FFTLog[26] algorithm to compute the complex integrals required (see Eq. (12)), a very efficient alternative to the brute force approach when the integrals involved contain Bessel functions. However, since the algorithm relies on the time-space separability of the considered kernels, PyCross cannot compute CMB angular power spectra and instead uses directly outputs from CLASS. The code has no Fisher computation capabilities; it was mainly used in the present work as a means to assess to what extent the calculation of angular power spectra may be impacted by the chosen method of integration, given the large-scale nature of the LSS×CMB cross-correlation (and thus its sensitivity to approximations such as the Limber one).

TomoCelle[27] is a code written in IDL with an interface to CAMB for the 3D power spectrum estimation, and with a FFTLog Fortran routine for the auto and CMB-cross angular power spectra computation. The code supports any arbitrary selection function for the survey with any generic $b(k, z)$ galaxy bias dependence. However, it lacks a Fisher-matrix module, and its use was restricted to the comparison and validation of angular power spectra.

4.2. Code comparison and validation

A crucial step in any Fisher forecast analysis is to verify the accuracy of the numerical codes involved at every step of the computation of the final constraints. The use of multiple distinct codes (at least two) computing the same quantities is essential in order to validate them. In this context, we aimed our comparison efforts towards three main computed quantities: (i) theoretical observables, namely the angular power spectra associated with the *Euclid*, CMB, and *Euclid*×CMB probes, which involve the various Boltzmann codes used here in their computation; (ii) their derivatives with respect to our parameters of interest (both cosmological and nuisance types), which notably relies on some arbitrary choices in the numerical differentiation method adopted; and (iii) the computation of the final Fisher matrices themselves, mostly involving matrix algebra.

We assumed that CMB observables did not require too much scrutiny from our side. Indeed, in all the codes involved in the present work, the computation of these observables is taken care of by very well-tested Boltzmann codes (namely CAMB and CLASS), which have been the subject of dedicated validation studies in the literature (see e.g., Lesgourgues 2011; Howlett et al. 2012). The codes were used mostly 'out of the box', with precision settings high enough to not require further validation.

Regarding *Euclid* observables, the outputs of the two aforementioned IST-validated codes CosmicFish and CosmoSIS acted as benchmarks for validating the *Euclid* observables computed by the four other codes introduced in the previous section. Agreement was reached at the 0.1–1% level over the whole range of relevant multipoles and probes considered here. The comparison of *Euclid*×CMB observables was carried out between the four codes specifically developed for the present work and reached a similar level of validation, despite their non-negligible conceptual and practical differences.

---

[26] `jila.colorado.edu/~ajsh/FFTLog`
[27] Contact: C. Hernández-Monteagudo.

Table 4. Predicted constraints on cosmological parameters from *Euclid*.

Model	$\Omega_{b,0}$	$\Omega_{m,0}$	n_s	h	σ_8	$\Omega_{DE,0}$	w_0	w_a	γ
Euclid pessimistic									
Flat ΛCDM	0.025	0.0065	0.0052	0.0036	0.0031	...	...	...	...
Non-flat ΛCDM	0.026	0.0065	0.0054	0.0042	0.0032	0.0099	...	...	...
Flat w_0w_aCDM	0.031	0.011	0.0056	0.0046	0.0045	...	0.038	0.14	...
Non-flat w_0w_aCDM	0.031	0.011	0.0056	0.0047	0.0047	0.025	0.039	0.22	...
Flat $w_0w_a\gamma$CDM	0.038	0.015	0.0059	0.0047	0.0050	...	0.039	0.14	0.015
Non-flat $w_0w_a\gamma$CDM	0.038	0.015	0.0059	0.0047	0.0055	0.025	0.039	0.23	0.016
Euclid optimistic									
Flat ΛCDM	0.011	0.0025	0.0015	0.0011	0.0012	...	...	...	...
Non-flat ΛCDM	0.011	0.0031	0.0018	0.0014	0.0012	0.0064	...	...	...
Flat w_0w_aCDM	0.013	0.0053	0.0019	0.0014	0.0019	...	0.021	0.073	...
Non-flat w_0w_aCDM	0.013	0.0053	0.0019	0.0015	0.0020	0.011	0.021	0.086	...
Flat $w_0w_a\gamma$CDM	0.017	0.0083	0.0022	0.0016	0.0024	...	0.021	0.073	0.0077
Non-flat $w_0w_a\gamma$CDM	0.018	0.0085	0.0022	0.0016	0.0027	0.011	0.021	0.092	0.0086

Notes. We report here the predicted constraints on cosmological parameters from the joint analysis of all *Euclid* probes (GCs+WL+GCp+GCp×WL), expressed as the ratio of marginalised 1σ uncertainties over their corresponding fiducial values (cf. Table 1). We note that for w_a, whose fiducial value is 0, we directly quote the 1σ uncertainties. Because *Euclid* observables alone cannot constrain τ, it is absent from this table. Values shown here are not exactly identical to (but within an acceptable range of) the same quantities reported in EC20, due to small numerical differences between the codes used.

Considering the very large number of angular power spectra considered as observables (namely 276) and multipole range (up to $\ell = 5000$), multiplied by the numerous parameters involved in our analyses (10 cosmological and 13 nuisance) a direct comparison of the derivatives among different codes proved impracticable and mostly unnecessary. We thus decided to validate those derivatives directly at the level of the Fisher matrices. Such an approach can be further justified by the observation that a potentially large relative difference between codes in the derivative of a given spectrum may not have any influence at all on the final Fisher forecasts, especially if the covariance of the corresponding spectrum is much larger that its derivative. We were able to reach agreement on the final marginalised constraints on parameters, all within 10% of each other (a criterion adopted by EC20) when compared to the *Euclid*-only results of EC20, and when comparing the various internal codes used in our analysis.

5. Results

In this section, we present and discuss the results of the validated Fisher matrix codes for the cosmological parameters under study, namely

$$\{\Omega_{b,0},\ \Omega_{m,0},\ h,\ n_s,\ \sigma_8,\ \tau,\ \Omega_{DE,0},\ w_0,\ w_a,\ \gamma\}\,, \tag{19}$$

whose fiducial values are reported in Table 1, as well as the nuisance parameters (the 10 galaxy bias and three IA parameters). More precisely, we explore the six cosmological 'cases' considered by EC20, namely: (i) a flat universe with cosmological constant (ΛCDM); (ii) non-flat ΛCDM; (iii) flat with time-varying DE equation of state (w_0w_aCDM); (iv) non-flat w_0w_aCDM; (v) flat with time-varying DE and phenomenological modification of gravity ($w_0w_a\gamma$CDM); and (vi) non-flat $w_0w_a\gamma$CDM. The main objective of the present work is to quantify the benefits of the combination of *Euclid* probes with CMB data. We thus first show as a reference in Table 4 the precision reached on all the aforementioned parameters when *Euclid*-only probes are considered, namely GCs, GCp, WL, and GCp×WL. We recall that all computations required to obtain those results were carried out using a dedicated suite of codes, stemming from the recipes of EC20

– with the exception of GCs, which was added directly at the Fisher matrix level as an independent probe, using the official public Euclid Collaboration matrices.

We present first in Fig. 4 the improvements resulting from the combination of *Euclid* probes with a subset of the CMB observables, namely the CMB lensing signal only. This subset is indeed a natural choice for combination with large-scale galaxy surveys, since it represents a counterpart in the CMB to late-Universe tracers of the matter distribution. Moreover, it is often considered a somewhat cleaner probe of matter, and it is hoped that it will alleviate some of the tracer-related systematics that plague galaxy surveys. We then present in Fig. 5 the outcome of a complete joint *Euclid*×CMB analysis (with all CMB probes added), showcasing the constraining power of the full combination.

In the aforementioned figures, for each cosmological and nuisance parameter the colour coding reflects the percentage improvement defined as

$$\left(\frac{\sigma_{\mathrm{before}}}{\sigma_{\mathrm{after}}} - 1\right) \times 100\,, \tag{20}$$

where σ_{before} and σ_{after} are, respectively, the 1σ uncertainties before and after adding CMB-related constraints, while the number in each square corresponds to the factor of improvement, namely

$$\frac{\sigma_{\mathrm{before}}}{\sigma_{\mathrm{after}}}\,. \tag{21}$$

5.1. Euclid and CMB lensing combination

As can be seen in Fig. 4, the combination and cross-correlation of *Euclid* probes with CMB lensing noticeably improves the constraints on the nuisance parameters, in particular the ones related to intrinsic alignments in the pessimistic *Euclid* scenario. There, the improvement on the parameters $\mathcal{A}_{\mathrm{IA}}$, η_{IA}, and β_{IA} ranges, respectively, from 2.7%, 1.9%, and 5.1% to 9.5%, 7.7%, and 15.6% across all considered cosmological models. Those
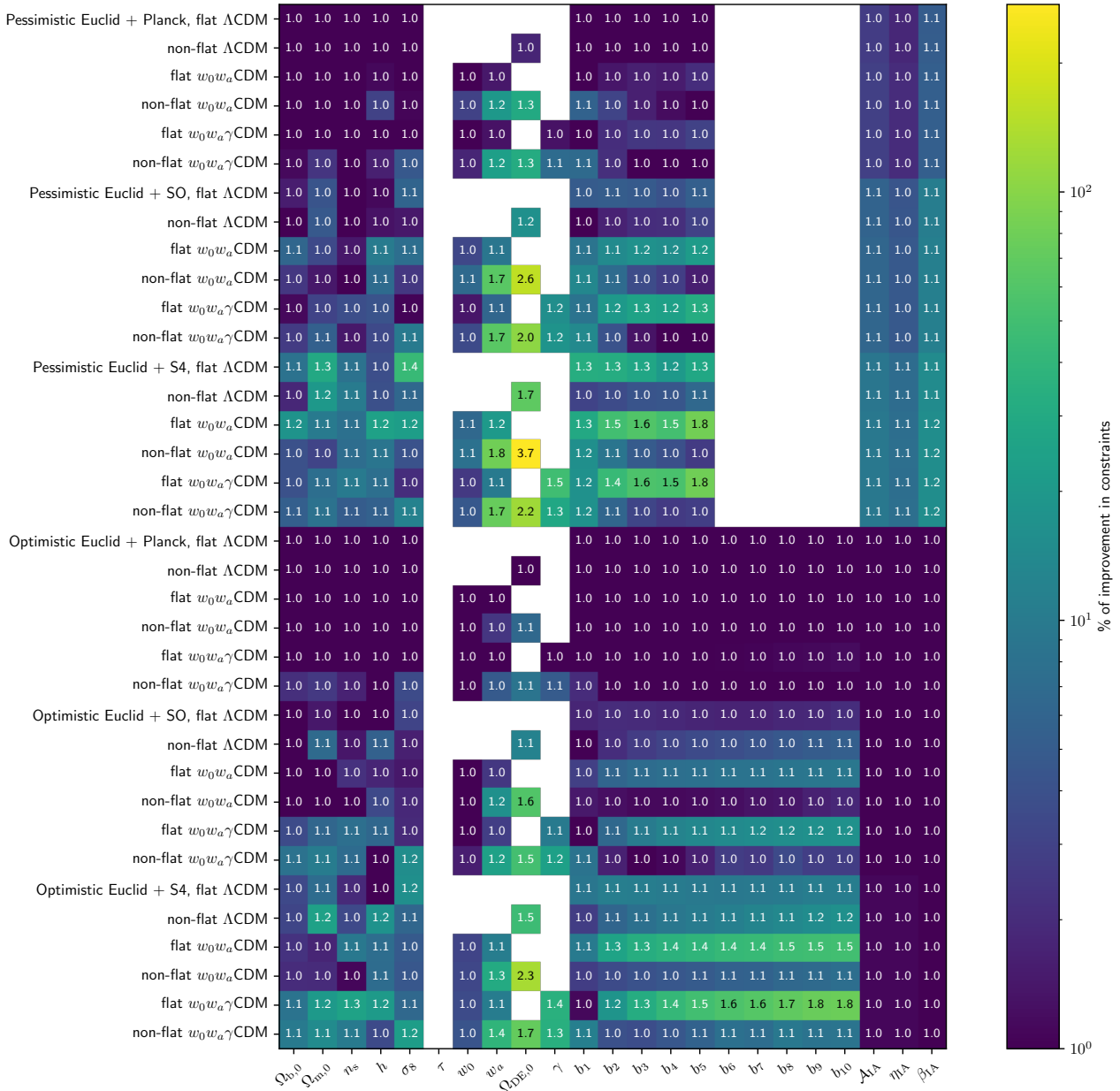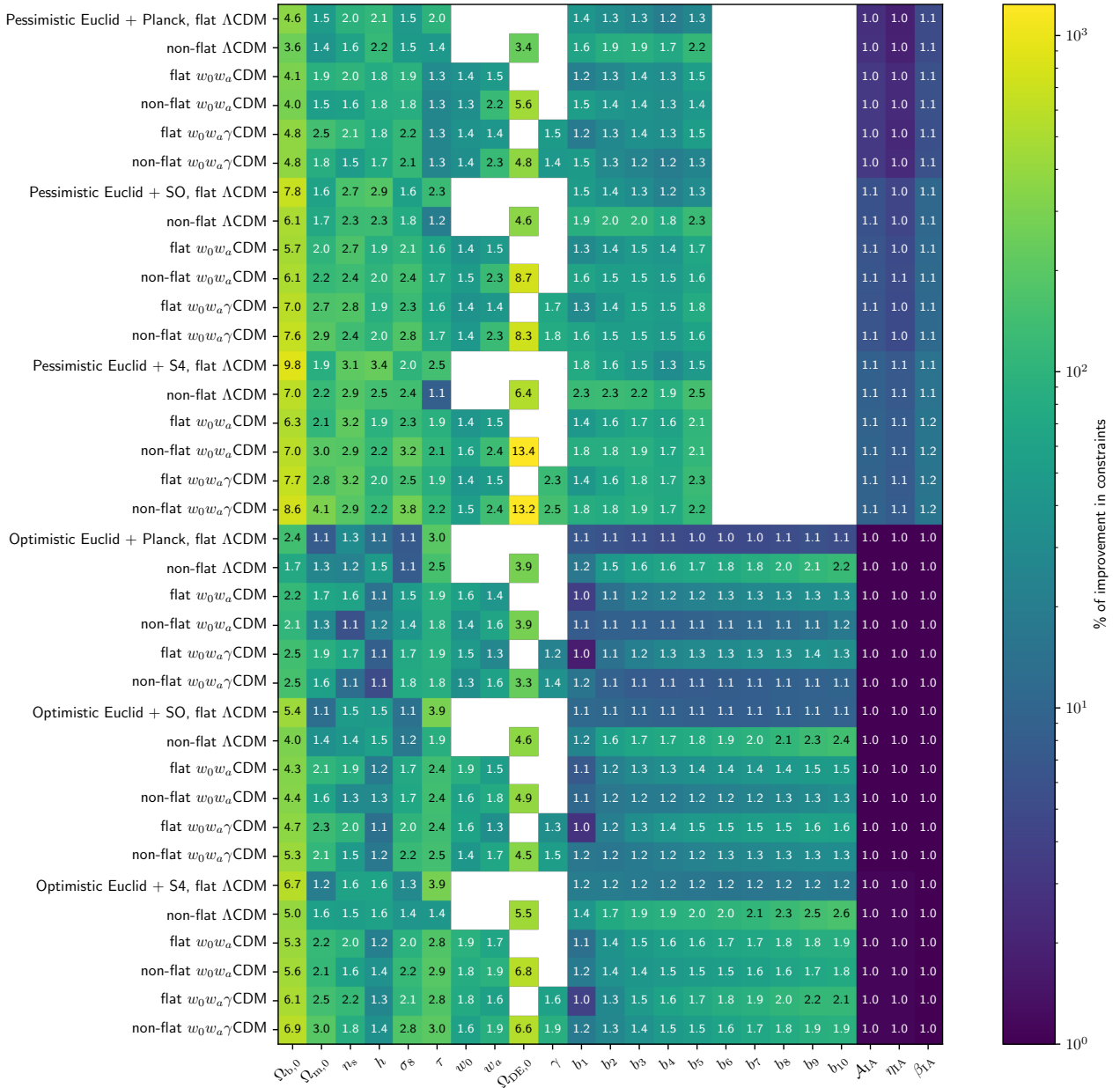
Fig. 4. Predicted improvements on parameter constraints after adding CMB lensing data to *Euclid*, including all cross-correlations, for all scenarios (cosmological models and survey specifications) considered in the present study. Colours indicate the percentage (cropped below 1%) of improvement in constraints, while numbers show the factors in the uncertainties reduction (see Sect. 5.1 for details).

improvements stem from the kernel overlap between CMB lensing and galaxy WL; since the CMB lensing measurement is not affected by IA, its combination and cross-correlation with WL probes allows us to break degeneracies introduced by the IA nuisance parameters, incidentally improving the constraints on those parameters. A similar effect can be observed for the constraints on galaxy bias parameters, with improvements reaching up to 83%. The improvements are especially seen on the high-redshift bias parameters in the *Euclid* optimistic case; the cross-correlation of galaxy density and CMB lensing is probing the peak of the CMB lensing kernel ($z \sim 2$) hence maximising its impact in the analysis at those redshifts. Unsurprisingly, the combination of *Euclid* with *Planck* observables is the least constraining. This comes from the fact that the CMB lensing information, dominant at small angular scales, cannot be optimally retrieved from *Planck*'s low-resolution data. On the other hand,

the lensing data obtained by the more advanced CMB facilities will provide more information to counteract the degeneracies introduced by intrinsic alignment.

For cosmological parameters, the joint analysis with lensing from SO – and even more so from a CMB-S4-like survey – improves the constraints the most as expected, especially in comparison to the *Euclid* pessimistic-only results. Parameters of the extended models particularly benefit from the combination, with the uncertainties on curvature being reduced by a factor of 3.7 at most, while the constraints on the MG parameter γ can be improved by 50%. DE parameters (w_0, w_a) are overall affected to a somewhat lesser extent, but still reach improvements of up to 80%, cf. w_a in the non-flat case compared to the pessimistic *Euclid*-only case. The standard set of cosmological parameters shows an improvement mainly when a CMB-S4-like survey is considered, with an average of 11% (maximum 44%) for

Fig. 5. Predicted improvements on parameter constraints after adding all CMB probes to *Euclid*, including all cross-correlations, for all scenarios (cosmological models and survey specifications) considered in the present study. Conventions are identical to those of Fig. 4. We note that, for the optical depth τ, since *Euclid* alone is not able to constrain this parameter, we show instead the predicted improvement after adding *Euclid* to CMB data.

pessimistic *Euclid* and 9% (maximum 25%) for the optimistic case, while other CMB scenarios show a below 5% average improvement.

5.2. Full Euclid×CMB joint analysis

In this second part of our analysis, we take into account all CMB probes (temperature, polarisation and lensing) and all their cross-correlations with *Euclid* in the data vector of the Fisher analysis. Figure 5 summarises our forecasts for the full *Euclid*×CMB joint analysis by showing the improvements in constraints compared to the case where only *Euclid* probes are considered.

The addition of CMB probes significantly improves the constraints on cosmological parameters in all the cosmological cases considered. We observe that in most scenarios, $\Omega_{b,0}$ and $\Omega_{DE,0}$

are the parameters that are best improved as a result of the joint analysis. In the case of $\Omega_{b,0}$, the factor of improvement across the different cosmological models ranges from 1.7 when *Planck* is added to optimistic *Euclid* results, and up to 9.8 when CMB-S4-like data are combined with a more pessimistic scenario for *Euclid* (with an overall average factor of 5.3). This improvement is likely due to the fact that the shape of the CMB power spectrum and relative amplitudes of the acoustic peaks are highly sensitive to baryon density. For $\Omega_{DE,0}$, the improvement factor across cosmological models ranges between 3.3 and 13.4 (average 6.2, roughly twice as constraining as the addition of CMB lensing alone), echoing the constraining power of the CMB on curvature. On the contrary, the Hubble parameter h is among the ones showing the least improvement, with an average factor of improvement of 1.7 (maximum 3.4). This indicates
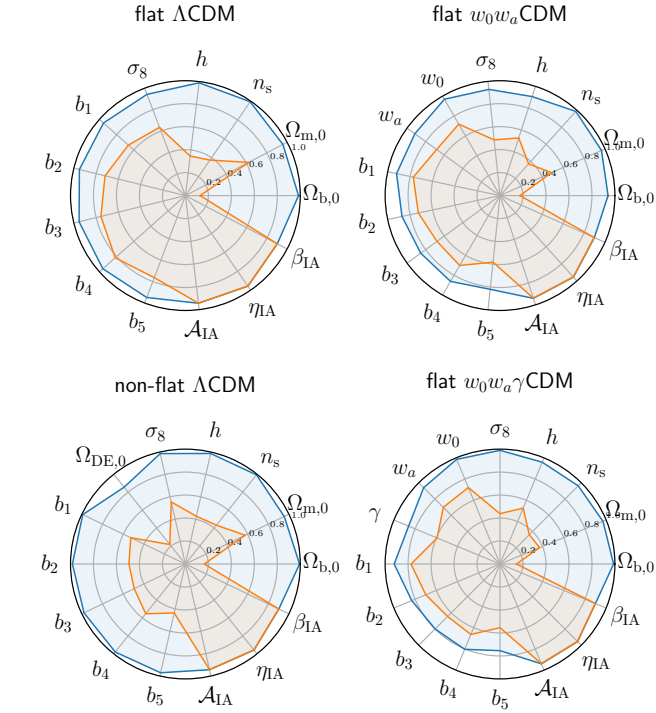
Fig. 6. Ratio of predicted 1σ uncertainties (see end of Sect. 5.2) showing how constraints are tightened after adding CMB lensing (blue) or all CMB probes (orange) when compared to the *Euclid*-only constraints (black outer rim), assuming a pessimistic *Euclid* scenario and SO-like CMB data, for four selected cosmological models (*from top to bottom, left to right*: flat ΛCDM; flat $w_0 w_a$CDM; non-flat ΛCDM; and flat $w_0 w_a \gamma$CDM).

Fig. 7. Predicted 1D and 2D marginalised distributions for the w_0–w_a and/or γ parameters, for four cosmological model: flat $w_0 w_a$CDM (*top left*); non-flat $w_0 w_a$CDM (*top right*); flat $w_0 w_a \gamma$CDM (*middle and bottom left*); and non-flat $w_0 w_a \gamma$CDM (*middle and bottom right*). This is for the same scenario as Fig. 6, using the same colour coding (where *Euclid*-only constraints are here in dashed black). Each plot is accompanied by the corresponding FoM or 1σ uncertainties.

that the *Euclid* main probes, GC and WL, are already powerful at constraining the background evolution of the Universe, and so CMB data do not add much more information. Moreover, CMB observables depend on h mostly through the location of the acoustic peaks, namely the angular size of the sound horizon at recombination, which is an integrated quantity and only directly related to h in the simplest models. Thus, the introduction of additional cosmological parameters – also entering the computation of the angular size – induces degeneracies that further reduce the constraining power of the CMB on h. Constraints on the other parameters of extensions to the baseline cosmological model, namely w_0, w_a and γ, show a (relatively) moderate improvement with respect to the *Euclid*-alone constraints, with an average factor of 1.6 (maximum 2.5). The full joint analysis with CMB provides on average an additional improvement factor of 1.4 (maximum 1.9) on these parameter constraints compared to the gains from adding CMB lensing alone.

Lastly, we underline the special status of one of the parameters considered in Fig. 5, namely the optical depth of reionisation. Indeed, since the late-Universe probes of *Euclid* are not sensitive to τ (and thus cannot constrain it) we show instead in the corresponding column the converse, namely the predicted improvement from the joint *Euclid*×CMB analysis compared to CMB-only constraints on τ. The resulting gains range from a very modest 1.09 to an impressive 3.9 factor (average 2.1). The trends in those improvements are easily understood: the optimistic *Euclid* scenario has a larger effect than the pessimistic one, and the worse the CMB specs are, the greater the amplitude of the improvement. These results originate mostly from the degeneracy between τ and the amplitude of perturbations A_s in CMB studies, which is broken when adding the tight constraints

on σ_8 from large-scale surveys. The case of τ illustrates the two-way nature of the gains expected from the *Euclid*×CMB joint analysis, and means that we expect to break other CMB-related degeneracies in the future (e.g., the ones involving the tensor-to-scalar ratio), as well as probe-specific systematic effects.

Overall, we find that the standard cosmological model and its extensions benefit greatly from the joint analysis of *Euclid* and the CMB, in terms of precision on the measured parameters. It also appears quite clear that, as was to be expected, the addition of CMB constraints is more helpful for the pessimistic *Euclid* scenario than for the optimistic one. Finally, we note that a CMB-S4-like experiment is obviously the source of the highest improvements when combined with *Euclid* results, given its superior resolution and sensitivity.

For further illustration purposes, Fig. 6 highlights a particular scenario from Figs. 4 and 5, namely an SO-like CMB survey combined with a pessimistic *Euclid* survey, for four of our six cosmological models. The results are presented in the form of

Table 5. Predicted constraints on cosmological parameters from the joint *Euclid*×CMB analysis.

Model	$\Omega_{b,0}$	$\Omega_{m,0}$	n_s	h	σ_8	$\Omega_{DE,0}$	w_0	w_a	γ
	After combination with CMB lensing								
Flat ΛCDM	0.025	0.0062	0.0052	0.0036	0.0029	...	...	...	...
Non-flat ΛCDM	0.026	0.0062	0.0054	0.0042	0.0032	0.0085	...	...	...
Flat $w_0\,w_a$CDM	0.029	0.010	0.0055	0.0041	0.0042	...	0.036	0.13	...
Non-flat $w_0\,w_a$CDM	0.030	0.011	0.0056	0.0044	0.0046	0.0096	0.037	0.13	...
Flat $w_0\,w_a\,\gamma$CDM	0.038	0.015	0.0057	0.0045	0.0049	...	0.038	0.14	0.013
Non-flat $w_0\,w_a\,\gamma$CDM	0.037	0.014	0.0058	0.0046	0.0050	0.012	0.038	0.14	0.013
	Full *Euclid*×CMB joint analysis								
Flat ΛCDM	0.0032	0.0040	0.0020	0.0012	0.0019	...	...	...	...
Non-flat ΛCDM	0.0043	0.0038	0.0024	0.0018	0.0018	0.0022	...	...	...
Flat $w_0\,w_a$CDM	0.0054	0.0053	0.0021	0.0024	0.0022	...	0.027	0.099	...
Non-flat $w_0\,w_a$CDM	0.0050	0.0049	0.0024	0.0023	0.0019	0.0029	0.026	0.096	...
Flat $w_0\,w_a\,\gamma$CDM	0.0055	0.0056	0.0021	0.0025	0.0022	...	0.028	0.10	0.0088
Non-flat $w_0\,w_a\,\gamma$CDM	0.0051	0.0052	0.0024	0.0023	0.0020	0.0031	0.027	0.10	0.0088

Notes. We report here the predicted constraints on cosmological parameters from the joint analysis of a pessimistic *Euclid* survey and SO-like CMB probes (CMB lensing only and full *Euclid*×CMB combination), expressed as the ratio of marginalised 1σ uncertainties over their corresponding fiducial values (same conventions as Table 4).

'radar' plots, which show this time the ratio of uncertainties

$$\frac{\sigma_{\text{after}}}{\sigma_{\text{before}}}, \tag{22}$$

namely the inverse of the ratios shown in Figs. 4 and 5. The distance from the centres of these plots is a visual representation of the 1σ uncertainty on all parameters of our analysis, where a length of one corresponds to the *Euclid*-only constraints. We observe here once again how adding CMB lensing information (blue lines) affects mostly the nuisance parameters and extended models parameters, whereas the addition of all CMB probes has a more dramatic overall effect on all parameters for all models. Some additional visualisation of our results is presented in Fig. 7: for the same aforementioned scenario (pessimistic *Euclid* + SO), we plot the 2D marginalised constraints in the w_0–w_a plane, and the 1D marginalised distribution for the MG parameter γ. Each plot contains in its legend either the corresponding 'figures of merit' (FoM, proportional to the inverse of the area of the ellipse of constraints, see EC20 for an exact definition) in the case of w_0–w_a constraints, or the 1σ uncertainties for γ. The FoM figures are particularly relevant because they represent one of the main expected results of *Euclid*, namely constraints on the equation of state of the elusive DE. Our plots illustrate in particular how, even though CMB data by themselves do not provide much constraints on the DE equation of state, the improvements on the determination of other parameters can still yield a significant shrinkage of the 2D contours, thanks to correlations between parameters. The effect is particularly visible for the non-flat models, where the substantial CMB constraints on curvature play a large role in the improvements, even when only adding CMB lensing data. The full numerical results for this particular scenario are shown in Table 5.

6. Conclusions

Euclid will revolutionise our vision of the Universe by mapping its matter distribution and providing us with exquisite measurements of its main probes, namely WL and GC, hence probing the nature of the accelerated expansion. At the same time, a wealth of data will be available from large surveys ranging from optical

(e.g., *Vera Rubin* Observatory) to radio (e.g., the Square Kilometre Array) and the millimetre (SO).

In this context, the combination and cross-correlation of the upcoming *Euclid* and CMB survey data will be of prime importance for cosmological analyses. In preparation for this synergetic data exploitation, we have conducted a forecast analysis on the precision achievable on the most important cosmological parameters, including the ones describing DE and MG. To do so, we have used a standard Fisher formalism, as well as a posterior-fitting approach based on actual CMB data, assuming nominal specifications of the current and future surveys. For *Euclid*, we have set up our forecasting pipeline in a consistent and complementary manner with respect to recently published forecasts on *Euclid*-specific probes (EC20) namely GC, WL, and their cross-correlation. In terms of CMB specifications, we have considered the cases of a *Planck*-like survey, the SO, and the CMB-S4 experiment.

In our analysis, we derived constraints for a baseline model, the ΛCDM cosmological model with (minimal) massive neutrinos, described by six cosmological parameters. We also explored: a possible non-zero curvature; a redshift-dependent DE equation of state; and a phenomenological description of MG. In addition, we considered 13 nuisance parameters, consistent with the forecasts previously presented by the Euclid Consortium (EC20). We have evaluated the expected impact of the combination and cross-correlation of *Euclid* with CMB data in terms of improvement factors with respect to the pure *Euclid* constraining capabilities.

We found that the addition of CMB data (and their cross-correlations with *Euclid* observables) helps substantially in reducing the impact of nuisance parameters on cosmological constraints, leading for example to an improvement of up to 15% on intrinsic alignment parameters and 2.6 times smaller uncertainties on galaxy bias. The joint *Euclid* and CMB analysis also leads to a substantial improvement on all cosmological parameters of the standard ΛCDM model, but with varying amplitude, noting for example the higher gains for $\Omega_{b,0}$, but the lower gains for the reduced Hubble parameter h. Depending on the cosmological model considered (e.g., when a time-varying DE equation of state, a non-zero curvature, or a phenomenological MG are added), the improvement in the constraints ranges from tens

of percent to factors of a few. In particular, the overall improvement in the w_0–w_a constraints for all three CMB experiments considered here implies an increase in the corresponding figure-of-merit by a factor two and up to almost seven in certain cases (cf. Fig. 7).

Finally, we stress that these results were obtained in configurations where the full complexity and the completeness of CMB and *Euclid* observables was not modelled. Indeed, among the numerous 'ingredients' that were not included, one can mention:

– Uncertainties on the galaxy redshift distribution, as well as on the parameters of the photometric error modelling (all fixed to their fiducial values here);
– Scale dependence of the galaxy bias, especially on non-linear scales;
– Correlations between GCs and all other probes considered;
– BAO reconstruction as an additional probe extracted from the spectroscopic data;
– Magnification bias and redshift-space distortions in the GCp analysis;
– Additional non-Gaussian terms in the covariances (thus reducing the constraining power of the considered probes), for example due to non-linear effects or the super-sample covariance.

The inclusion of some of those points in the analysis could significantly improve the *Euclid*-only constraints, while some could also severely degrade them. For these latter cases the combination with CMB data could significantly (and positively) affect the final results. Despite this, our results shown here in a more ideal setting not only confirm and highlight the benefits of combining and cross-correlating *Euclid* with the CMB, but also show how powerful cross-correlations are for actual data analysis. On the basis of these results, future work will consider a more exhaustive set of non-standard cosmological models, and the validation of these forecasts by means of an end-to-end pipeline involving more realistic instrumental effects.

References

Abazajian, K. N., Adshead, P., Ahmed, Z., et al. 2016, ArXiv eprints [arXiv:1610.02743]
Abbott, T. M. C., Abdalla, F. B., Allam, S., et al. 2018a, ApJS, 239, 18
Abbott, T. M. C., Abdalla, F. B., Alarcon, A., et al. 2018b, Phys. Rev. D, 98, 043526
Abbott, T. M. C., Allam, S., Andersen, P., et al. 2019, ApJ, 872, L30
Ade, P., Aguirre, J., Ahmed, Z., et al. 2019, J. Cosmol. Astropart. Phys., 2019, 056
Aghanim, N., Majumdar, S., & Silk, J. 2008, Rep. Prog. Phys., 71, 066902
Akeson, R., Armus, L., Bachelet, E., et al. 2019, ArXiv eprints [arXiv:1902.05569]
Alam, S., Ata, M., Bailey, S., et al. 2017, MNRAS, 470, 2617
Alam, S., Aubert, M., Avila, S., et al. 2021, Phys. Rev. D, 103, 083533
Amendola, L., Appleby, S., Bacon, D., et al. 2013, Liv. Rev. Relativ., 16, 6
Ballardini, M., Finelli, F., Fedeli, C., & Moscardini, L. 2016, J. Cosmol. Astropart. Phys., 1610, 041 [Erratum: JCAP1804, no.04, E01(2018)]
Ballardini, M., Matthewson, W. L., & Maartens, R. 2019a, MNRAS, 489, 1950
Ballardini, M., Paoletti, D., Finelli, F., et al. 2019b, MNRAS, 482, 2670
Baxter, E. J., Omori, Y., Chang, C., et al. 2019, Phys. Rev. D, 99, 023508
Bellomo, N., Bernal, J. L., Scelfo, G., Raccanelli, A., & Verde, L. 2020, J. Cosmol. Astropart. Phys., 2020, 016
Bermejo-Climent, J. R., Ballardini, M., Finelli, F., & Cardone, V. F. 2020, Phys. Rev. D, 102, 023502
Bermejo-Climent, J. R., Ballardini, M., Finelli, F., et al. 2021, Phys. Rev. D, 103, 103502
Bianchini, F., Wu, W. L. K., Ade, P. A. R., et al. 2020, ApJ, 888, 119
Bird, S., Viel, M., & Haehnelt, M. G. 2012, MNRAS, 420, 2551
Blas, D., Lesgourgues, J., & Tram, T. 2011, J. Cosmol. Astropart., 2011, 034
Bonoli, S., Marín-Franch, A., Varela, J., et al. 2021, A&A, 653, A31
Bunn, E. F. 1995, Ph.D. Thesis, University of California, Berkeley, USA
Carron, J. 2013, A&A, 551, A88
Carron, J., & Lewis, A. 2017, Phys. Rev. D, 96, 063510
Chevallier, M., & Polarski, D. 2001, Int. J. Mod. Phys. D, 10, 213
Datta, R., Aiola, S., Choi, S. K., et al. 2019, MNRAS, 486, 5239
Dey, A., Schlegel, D. J., Lang, D., et al. 2019, AJ, 157, 168
Euclid Collaboration 2020, A&A, 642, A191
Hand, N., Leauthaud, A., Das, S., et al. 2015, Phys. Rev. D, 91, 062001
Hojjati, A., Pogosian, L., & Zhao, G.-B. 2011, J. Cosmol. Astropart., 2011, 005
Hojjati, A., Tröster, T., Harnois-Déraps, J., et al. 2017, MNRAS, 471, 1565
Holder, G. P., Viero, M. P., Zahn, O., et al. 2013, ApJ, 771, L16
Howlett, C., Lewis, A., Hall, A., & Challinor, A. 2012, J. Cosmol. Astropart., 2012, 027
Icaza-Lizaola, M., Vargas-Magaña, M., Fromenteau, S., et al. 2020, MNRAS, 492, 4189
Kahn, S. 2018, 42nd COSPAR Scientific Assembly, 42, E1.16-5-18
Kirk, D., Omori, Y., Benoit-Lévy, A., et al. 2016, MNRAS, 459, 21
Knox, L. 1995, Phys. Rev. D, 52, 4307
Lacasa, F., & Rosenfeld, R. 2016, J. Cosmol. Astropart., 2016, 005

Lahav, O., Lilje, P. B., Primack, J. R., & Rees, M. J. 1991, MNRAS, 251, 128

Laureijs, R., Amiaux, J., Arduini, S., et al. 2011, ArXiv eprints [arXiv:1110.3193]

Lesgourgues, J. 2011, ArXiv eprints [arXiv:1104.2934]

Lewis, A., & Challinor, A. 2006, Phys. Rep., 429, 1

Linder, E. V. 2003, Phys. Rev. Lett., 90, 091301

Linder, E. V. 2005, Phys. Rev. D, 72, 043529

Ma, Y.-Z., Van Waerbeke, L., Hinshaw, G., et al. 2015, J. Cosmol. Astropart., 2015, 046

Munshi, D., Namikawa, T., Kitching, T. D., et al. 2020, MNRAS, 493, 3985

Okamoto, T., & Hu, W. 2003, Phys. Rev. D, 67, 083002

Osato, K., Shirasaki, M., Miyatake, H., et al. 2020, MNRAS, 492, 4780

Particle Data Group 2020, Prog. Theor. Exp. Phys., 2020, 083C01

Percival, W. J. 2017, Phys. Today, 70, 32

Planck Collaboration I. 2016, A&A, 594, A1

Planck Collaboration XIII. 2016, A&A, 594, A13

Planck Collaboration V. 2020, A&A, 641, A5

Planck Collaboration VI. 2020, A&A, 641, A6

Planck Collaboration VIII. 2020, A&A, 641, A8

Polarbear Collaboration 2020, ApJ, 897, 55

Pozzetti, L., Hirata, C. M., Geach, J. E., et al. 2016, A&A, 590, A3

Prole, D. J., van der Burg, R. F. J., Hilker, M., & Davies, J. I. 2019, ArXiv eprints [arXiv:1910.14057]

Raveri, M., Martinelli, M., Zhao, G., & Wang, Y. 2016a, ArXiv eprints [arXiv:1606.06268]

Raveri, M., Martinelli, M., Zhao, G., & Wang, Y. 2016b, ArXiv eprints [arXiv:1606.06273]

Refregier, A., Amara, A., Kitching, T. D., et al. 2010, ArXiv eprints [arXiv:1001.0061]

Schmittfull, M., & Seljak, U. 2018, Phys. Rev. D, 97, 123540

Takahashi, R., Sato, M., Nishimichi, T., Taruya, A., & Oguri, M. 2012, ApJ, 761, 152

Tegmark, M., Taylor, A., & Heavens, A. 1997, ApJ, 480, 22

Vogeley, M. S., & Szalay, A. S. 1996, ApJ, 465, 34

Wang, Y., Bean, R., Behroozi, P., et al. 2019, BAAS, 51, 508

Yan, Z., van Waerbeke, L., Tröster, T., et al. 2021, A&A, 651, A76

Zuntz, J., Paterno, M., Jennings, E., et al. 2015, Astron. Comput., 12, 45

1 Université PSL, Observatoire de Paris, Sorbonne Université, CNRS, LERMA, 75014 Paris, France
e-mail: stephane.ilic@obspm.fr

2 CEICO, Institute of Physics of the Czech Academy of Sciences, Na Slovance 2, Praha 8, Czech Republic

3 Institut de Recherche en Astrophysique et Planétologie (IRAP), Université de Toulouse, CNRS, UPS, CNES, 14 Av. Edouard Belin, 31400 Toulouse, France

4 Université Paris-Saclay, CNRS, Institut d'astrophysique spatiale, 91405 Orsay, France

5 IFPU, Institute for Fundamental Physics of the Universe, Via Beirut 2, 34151 Trieste, Italy

6 SISSA, International School for Advanced Studies, Via Bonomea 265, 34136 Trieste, TS, Italy

7 INFN, Sezione di Trieste, Via Valerio 2, 34127 Trieste, TS, Italy

8 INAF-Osservatorio Astronomico di Trieste, Via G. B. Tiepolo 11, 34131 Trieste, Italy

9 Departamento de Astrofísica, Universidad de La Laguna, 38206 La Laguna, Tenerife, Spain

10 INAF-Osservatorio di Astrofisica e Scienza dello Spazio di Bologna, Via Piero Gobetti 93/3, 40129 Bologna, Italy

11 INFN-Bologna, Via Irnerio 46, 40126 Bologna, Italy

12 Center for Computational Astrophysics, Flatiron Institute, 162 5th Avenue, 10010 New York, NY, USA

13 Université de Genève, Département de Physique Théorique and Centre for Astroparticle Physics, 24 quai Ernest-Ansermet, 1211 Genève 4, Switzerland

14 INFN-Sezione di Bologna, Viale Berti Pichat 6/2, 40127 Bologna, Italy

15 Dipartimento di Fisica e Astronomia, Universitá di Bologna, Via Gobetti 93/2, 40129 Bologna, Italy

16 Dipartimento di Fisica 'Aldo Pontremoli', Universitá degli Studi di Milano, Via Celoria 16, 20133 Milano, Italy

17 INFN-Sezione di Milano, Via Celoria 16, 20133 Milano, Italy

18 Université de Paris, CNRS, Astroparticule et Cosmologie, 75013 Paris, France

19 Instituto de Astrofísica de Canarias, Calle Vía Làctea s/n, 38204 San Cristòbal de la Laguna, Tenerife, Spain

20 Centro de Estudios de Física del Cosmos de Aragón (CEFCA), Plaza San Juan, 1, planta 2, 44001 Teruel, Spain

21 Istituto Nazionale di Fisica Nucleare, Sezione di Ferrara, Via Giuseppe Saragat 1, 44122 Ferrara, Italy

22 Dipartimento di Fisica, Università di Roma Tor Vergata, Via della Ricerca Scientifica 1, Roma, Italy

23 INFN, Sezione di Roma 2, Via della Ricerca Scientifica 1, Roma, Italy

24 INAF-IASF Milano, Via Alfonso Corti 12, 20133 Milano, Italy

25 AIM, CEA, CNRS, Université Paris-Saclay, Université de Paris, 91191 Gif-sur-Yvette, France

26 Instituto de Física Teórica UAM-CSIC, Campus de Cantoblanco, 28049 Madrid, Spain

27 Institute of Space Sciences (ICE, CSIC), Campus UAB, Carrer de Can Magrans, s/n, 08193 Barcelona, Spain

28 Institut d'Estudis Espacials de Catalunya (IEEC), Carrer Gran Capitá 2-4, 08034 Barcelona, Spain

29 Dipartimento di Fisica e Scienze della Terra, Universitá degli Studi di Ferrara, Via Giuseppe Saragat 1, 44122 Ferrara, Italy

30 Aix-Marseille Univ, CNRS/IN2P3, CPPM, Marseille, France

31 Department of Astronomy, Cornell University, Ithaca, NY 14853, USA

32 Mullard Space Science Laboratory, University College London, Holmbury St Mary, Dorking, Surrey RH5 6NT, UK

33 Dipartimento di Fisica e Astronomia 'Augusto Righi' – Alma Mater Studiorum Universitá di Bologna, Viale Berti Pichat 6/2, 40127 Bologna, Italy

34 INFN-Padova, Via Marzolo 8, 35131 Padova, Italy

35 Dipartimento di Fisica e Astronomia 'G.Galilei', Universitá di Padova, Via Marzolo 8, 35131 Padova, Italy

36 Space Science Data Center, Italian Space Agency, via del Politecnico snc, 00133 Roma, Italy

37 Astrophysics Research Institute, Liverpool John Moores University, 146 Brownlow Hill, Liverpool L3 5RF, UK

38 Université St Joseph; UR EGFEM, Faculty of Sciences, Beirut, Lebanon

39 School of Physics and Astronomy, Queen Mary University of London, Mile End Road, London E1 4NS, UK

40 INFN-Sezione di Torino, Via P. Giuria 1, 10125 Torino, Italy

41 Dipartimento di Fisica, Universitá degli Studi di Torino, Via P. Giuria 1, 10125 Torino, Italy

42 INFN-Sezione di Roma, Piazzale Aldo Moro, 2 – c/o Dipartimento di Fisica, Edificio G. Marconi, 00185 Roma, Italy

43 INAF-Osservatorio Astronomico di Roma, Via Frascati 33, 00078 Monteporzio Catone, Italy

44 Jet Propulsion Laboratory, California Institute of Technology, 4800 Oak Grove Drive, Pasadena, CA 91109, USA

45 Max Planck Institute for Extraterrestrial Physics, Giessenbachstr. 1, 85748 Garching, Germany

46 Departamento de Física, FCFM, Universidad de Chile, Blanco Encalada 2008, Santiago, Chile

47 Institute of Cosmology and Gravitation, University of Portsmouth, Portsmouth PO1 3FX, UK

48 Universitäts-Sternwarte München, Fakultät für Physik, Ludwig-Maximilians-Universität München, Scheinerstrasse 1, 81679 München, Germany

49 INAF-Osservatorio Astrofisico di Torino, Via Osservatorio 20, 10025 Pino Torinese, TO, Italy

50 INFN-Sezione di Roma Tre, Via della Vasca Navale 84, 00146 Roma, Italy

51 Department of Mathematics and Physics, Roma Tre University, Via della Vasca Navale 84, 00146 Rome, Italy

52 INAF-Osservatorio Astronomico di Capodimonte, Via Moiariello 16, 80131 Napoli, Italy

53 Centro de Astrofísica da Universidade do Porto, Rua das Estrelas, 4150-762 Porto, Portugal

54 Instituto de Astrofísica e Ciências do Espaço, Universidade do Porto, CAUP, Rua das Estrelas, 4150-762 Porto, Portugal

55 Institut de Física d'Altes Energies (IFAE), The Barcelona Institute of Science and Technology, Campus UAB, 08193 Bellaterra, Barcelona, Spain

56 Department of Physics 'E. Pancini', University Federico II, Via Cinthia 6, 80126 Napoli, Italy

57 INFN section of Naples, Via Cinthia 6, 80126 Napoli, Italy

58 Dipartimento di Fisica e Astronomia 'Augusto Righi' – Alma Mater Studiorum Università di Bologna, Via Piero Gobetti 93/2, 40129 Bologna, Italy

59 INAF-Osservatorio Astrofisico di Arcetri, Largo E. Fermi 5, 50125 Firenze, Italy

60 Institut national de physique nucléaire et de physique des particules, 3 rue Michel-Ange, 75794 Paris Cédex 16, France

61 Centre National d'Etudes Spatiales, Toulouse, France

62 Institute for Astronomy, University of Edinburgh, Royal Observatory, Blackford Hill, Edinburgh EH9 3HJ, UK

63 Jodrell Bank Centre for Astrophysics, School of Physics and Astronomy, University of Manchester, Oxford Road, Manchester M13 9PL, UK

64 European Space Agency/ESRIN, Largo Galileo Galilei 1, 00044 Frascati, Roma, Italy

65 ESAC/ESA, Camino Bajo del Castillo, s/n., Urb. Villafranca del Castillo, 28692 Villanueva de la Cañada Madrid, Spain

66 Univ Lyon, Univ Claude Bernard Lyon 1, CNRS/IN2P3, IP2I Lyon, UMR 5822, 69622 Villeurbanne, France

67 Aix-Marseille Univ, CNRS, CNES, LAM, Marseille, France

68 Departamento de Física, Faculdade de Ciências, Universidade de Lisboa, Edifício C8, Campo Grande, 1749-016 Lisboa, Portugal

69 Instituto de Astrofísica e Ciências do Espaço, Faculdade de Ciências, Universidade de Lisboa, Campo Grande, 1749-016 Lisboa, Portugal

70 Department of Astronomy, University of Geneva, ch. d'Ecogia 16, 1290 Versoix, Switzerland

71 Department of Physics, Oxford University, Keble Road, Oxford OX1 3RH, UK

72 Istituto Nazionale di Astrofisica (INAF) – Osservatorio di Astrofisica e Scienza dello Spazio (OAS), Via Gobetti 93/3, 40127 Bologna, Italy

73 Istituto Nazionale di Fisica Nucleare, Sezione di Bologna, Via Irnerio 46, 40126 Bologna, Italy

74 INAF-Osservatorio Astronomico di Padova, Via dell'Osservatorio 5, 35122 Padova, Italy

75 INAF-Osservatorio Astronomico di Brera, Via Brera 28, 20122 Milano, Italy

76 Institute of Theoretical Astrophysics, University of Oslo, PO Box 1029 Blindern, 0315 Oslo, Norway

77 Leiden Observatory, Leiden University, Niels Bohrweg 2, 2333, CA Leiden, The Netherlands

78 von Hoerner & Sulger GmbH, SchloßPlatz 8, 68723 Schwetzingen, Germany

79 Max-Planck-Institut für Astronomie, Königstuhl 17, 69117 Heidelberg, Germany

80 Institut d'Astrophysique de Paris, 98bis Boulevard Arago, 75014 Paris, France

81 Department of Physics and Helsinki Institute of Physics, Gustaf Hällströmin katu 2, 00014 University of Helsinki, Finland

82 European Space Agency/ESTEC, Keplerlaan 1, 2201, AZ Noordwijk, The Netherlands

83 NOVA optical infrared instrumentation group at ASTRON, Oude Hoogeveensedijk 4, 7991 PD Dwingeloo, The Netherlands

84 Argelander-Institut für Astronomie, Universität Bonn, Auf dem Hügel 71, 53121 Bonn, Germany

85 Institute for Computational Cosmology, Department of Physics, Durham University, South Road, Durham DH1 3LE, UK

86 Université Côte d'Azur, Observatoire de la Côte d'Azur, CNRS, Laboratoire Lagrange, Bd de l'Observatoire, CS 34229, 06304 Nice cedex 4, France

87 California institute of Technology, 1200 E California Blvd, Pasadena, CA 91125, USA

88 Observatoire de Sauverny, Ecole Polytechnique Fédérale de Lausanne, 1290 Versoix, Switzerland

89 Department of Physics and Astronomy, University of Aarhus, Ny Munkegade 120, 8000 Aarhus C, Denmark

90 Perimeter Institute for Theoretical Physics, Waterloo, Ontario N2L 2Y5, Canada

91 Department of Physics and Astronomy, University of Waterloo, Waterloo, Ontario N2L 3G1, Canada

92 Centre for Astrophysics, University of Waterloo, Waterloo, Ontario N2L 3G1, Canada

93 Institute of Space Science, Bucharest 077125, Romania

94 Centro de Investigaciones Energéticas, Medioambientales y Tecnológicas (CIEMAT), Avenida Complutense 40, 28040 Madrid, Spain

95 Instituto de Astrofísica e Ciências do Espaço, Faculdade de Ciências, Universidade de Lisboa, Tapada da Ajuda, 1349-018 Lisboa, Portugal

96 Universidad Politécnica de Cartagena, Departamento de Electrónica y Tecnología de Computadoras, 30202 Cartagena, Spain

97 Kapteyn Astronomical Institute, University of Groningen, PO Box 800, 9700 AV Groningen, The Netherlands

98 Infrared Processing and Analysis Center, California Institute of Technology, Pasadena, CA 91125, USA

99 Dipartimento di Fisica – Sezione di Astronomia, Universitá di Trieste, Via Tiepolo 11, 34131 Trieste, Italy

100 INAF, Istituto di Radioastronomia, Via Piero Gobetti 101, 40129 Bologna, Italy

101 University of Lyon, UCB Lyon 1, CNRS/IN2P3, IUF, IP2I Lyon, France

102 INAF-Istituto di Astrofisica e Planetologia Spaziali, via del Fosso del Cavaliere, 100, 00100 Roma, Italy

103 Research Program in Systems Oncology, Faculty of Medicine, University of Helsinki, Helsinki, Finland

104 Department of Physics, PO Box 64, 00014 University of Helsinki, Finland

105 Helsinki Institute of Physics, University of Helsinki, Gustaf Hällströmin katu 2, Helsinki, Finland

106 Centre de Calcul de l'IN2P3, 21 avenue Pierre de Coubertin, 69627 Villeurbanne Cedex, France

107 Institut für Theoretische Physik, University of Heidelberg, Philosophenweg 16, 69120 Heidelberg, Germany

108 Zentrum für Astronomie, Universität Heidelberg, Philosophenweg 12, 69120 Heidelberg, Germany

109 INFN, Sezione di Lecce, Via per Arnesano, CP-193, 73100 Lecce, Italy

110 Department of Mathematics and Physics E. De Giorgi, University of Salento, Via per Arnesano, CP-I93, 73100 Lecce, Italy

111 Institute for Computational Science, University of Zurich, Winterthurerstrasse 190, 8057 Zurich, Switzerland

112 Department of Physics, University of Jyväskylä, PO Box 35 (YFL), 40014 Jyväskylä, Finland

113 Department of Physics and Astronomy, University College London, Gower Street, London WC1E 6BT, UK

114 School of Physics and Astronomy, Cardiff University, The Parade, Cardiff CF24 3AA, UK

Appendix A: Fitted-Fisher approach

A.1. Method

We describe in this subsection a method – thereafter referred to as the 'fitted-Fisher approach' – designed to combine a theoretical *Euclid* Fisher matrix with constraints from the actual CMB data and likelihood, more specifically in the context of *Planck*.

For models that are well constrained by *Planck* data – such as the minimal ΛCDM – the posterior distribution of cosmological parameters follows a multivariate Gaussian quite closely. One can thus summarise the constraints from the *Planck* data by extracting the mean and the covariance matrix of cosmological parameters directly from the samples of a previously computed Monte Carlo Markov chain. The inverse of such a matrix can then be interpreted as a 'fitted-Fisher matrix', which can then be added to other 'actual' Fisher matrices in order to emulate the addition of CMB constraints.

For models that are less constrained (e.g. *w*CDM, $w_0 w_a$CDM), one can fit the posterior distribution of the MCMC approximately with a multi-dimensional Gaussian and thus obtain the covariance matrix. This fit is performed in the vicinity of the *Euclid* fiducial values of the extra parameters (e.g. $w_0 = -1, w_a = 0$, etc). This ensures that the resulting mean, covariance and fitted-Fisher matrix most accurately reflect what the actual *Euclid + Planck* combination would yield if we assume that the true underlying model is the fiducial one chosen for the *Euclid* Fisher matrix.

A technical point in this approach is that one cannot in practice directly combine the *Euclid* Fisher matrix and the *Planck* fitted-Fisher matrix described above, since they are not 'evaluated' at the same point in the parameter space – the *Euclid* Fisher matrix is evaluated around an arbitrarily chosen fiducial point, whereas by construction the CMB fitted-Fisher matrix is evaluated around the point corresponding to the maximum of the

Planck likelihood. As a consequence, some care has to be taken when combining the two matrices, and the resulting combination has a third, different effective fiducial point. In practice, since the separation between the two fiducial points is small, we decided here to simply shift the *Planck* fitted-Fisher matrix to the *Euclid* fiducial point, thus simplifying the addition of the two sets of constraints.

We note that, by construction, this fitted-Fisher approach is incapable of incorporating the impact of any cross-correlation between CMB and *Euclid* observables, since they are being considered as purely independent from each other. This approach and its results are thus presented here as a study case in the broader context of the full *Euclid*×CMB combination, which traditional Fisher forecasts can assess.

A.2. Results and discussion

The results from the *Euclid* and real *Planck* data combination via the fitted-Fisher approach are summarised in Fig. A.1. We see a remarkable agreement when compared to the traditional Fisher formalism (cf. Fig. 5); the two methods show similar trends and orders of magnitude for factors of improvements, across all data combinations and cosmological models considered. We note that, since we fitted the available posteriors of publicly available *Planck* chains,[28] the analysis is restricted to only three of our six models (namely flat ΛCDM, non-flat ΛCDM and flat $w_0 w_a$CDM). We acknowledge several causes that could explain the observed (relatively) small differences between the two methods, including the fact that the fitted-Fisher approach does not account for the covariance between *Planck* and *Euclid* (thus potentially overestimating some constraints) and the fact that our effective approach in defining the specifications of the *Planck*-like survey in the traditional Fisher approach may result in non-trivial deviations from the true *Planck* survey characteristics.
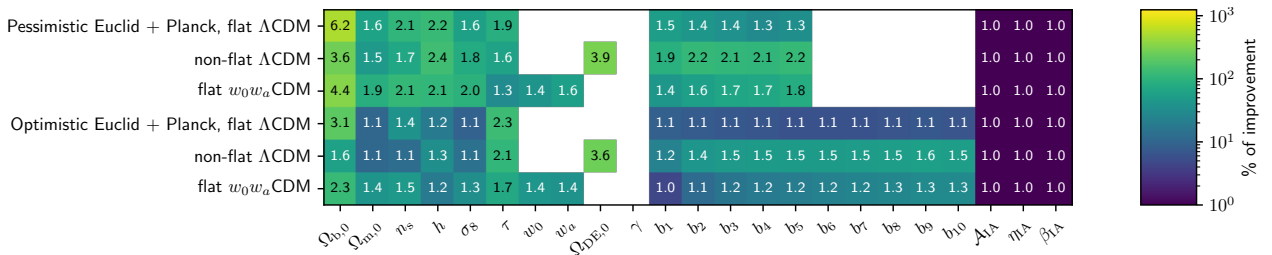
Fig. A.1. Predicted improvements on parameter constraints after adding *Planck* CMB data to *Euclid* via the fitted-Fisher approach. Conventions are identical to Fig. 4 and with the same remark for τ as in Fig. 5.

---

28 pla.esac.esa.int/pla